Spatially dispersed synapses yield sharply-tuned place cell responses through dendritic spike initiation

Reshma Basak and Rishikesh Narayanan[*]

Cellular Neurophysiology Laboratory, Molecular Biophysics Unit, Indian Institute of Science, Bangalore 560012, India.

*Correspondence to:

Rishikesh Narayanan, Ph.D.,
Molecular Biophysics Unit,
Indian Institute of Science,
Bangalore 560 012, India.
e-mail: rishi@mbu.iisc.ernet.in
Phone: +91-80-22933372

Abbreviated title: Dispersed synapses yield sharp place-cell tuning

Keywords: Active dendrites, computational model, dendritic spikes, hippocampus, place cells, synaptic clustering

CONFLICT OF INTEREST
The authors declare no conflict of interest.

AUTHOR CONTRIBUTIONS
R.B and R. N. designed experiments; R.B. performed experiments and carried out data analysis; R.B. and R. N. co-wrote the paper.

ABSTRACT

The literature offers evidence for a critical role of spatially-clustered iso-feature synapses in eliciting dendritic spikes essential for sharp feature selectivity, with apparently contradictory evidence demonstrating spatial dispersion of iso-feature synapses. Here, we reconcile this apparent contradiction by demonstrating that the generation of dendritic spikes, the emergence of an excitatory ramp in somatic voltage responses and sharp tuning of place-cell responses are all attainable even when iso-feature synapses are randomly dispersed across the dendritic arbor. We found this tuning sharpness to be critically reliant on dendritic sodium and transient potassium channels and on N-methyl-D-asparate receptors. Importantly, we demonstrate that synaptic potentiation targeted to afferents from one specific place field is sufficient to effectuate place-field selectivity even when intrinsically disparate neurons received randomly dispersed afferents from multiple place-field locations. These conclusions proffer dispersed localization of iso-feature synapses as a strong candidate for achieving sharp feature selectivity in neurons across sensory-perceptual systems.

2

A prominent hypothesis spanning several perceptual systems implicates spatially clustered synapses in the generation of dendritic spikes that mediate sharply-tuned neuronal responses to input features (Losonczy et al., 2008; Govindarajan et al., 2011; Makino and Malinow, 2011; Takahashi et al., 2012; Winnubst and Lohmann, 2012; DeBello et al., 2014; Druckmann et al., 2014; Wilson et al., 2016). On the other hand, there are significant lines of evidence, spanning several perceptual systems, for similarly-tuned synaptic inputs to be dispersed across the dendritic arbor (Jia et al., 2010; Chen et al., 2011; Varga et al., 2011; Hill et al., 2013; Grienberger et al., 2015; Domnisoru and Tank, 2016). How do we reconcile these apparently contradictory observations where spatial clustering is postulated to be required for eliciting dendritic spikes, and synaptic localization is shown to dispersed? Additionally, a predominant dogma on pyramidal cell neurophysiology is that linear or supralinear modes of operation are respectively preferred when synapses are dispersed or clustered, where the supralinear mode of operation recruits dendritic spikes owing to cooperativity among concomitantly activated synaptic inputs (Grienberger et al., 2015). Is spatial clustering of synapses an essential component for the expression of concomitantly active synaptic inputs towards the generation of dendritic spikes? Are spatial clustering of synapses and dendritic spikes essential in achieving sharp tuning to input features? How do the different voltage-gated ion channels and synaptic receptors that are expressed in the dendritic arbor of pyramidal neurons contribute to sharp tuning to input features?

In this conductance-based morphologically-precise computational study, we tested the hypothesis on the link between spatially clustered synapses and sharply tuned responses by systematically analyzing the impact of distinct synaptic and channel

3

localization profiles on sharpness of spatial tuning in hippocampal pyramidal neurons. We found that sharply-tuned firing responses were achieved in models where synapses were all clustered on the soma or were randomly dispersed across the dendritic arbor, but not in cases where the same set of synapses were localized to one or two obliques. Strikingly, dendritic spikes were more prevalent when synapses were randomly dispersed, with sharpness of spatial tuning mediated by the generation and propagation of dendritic spikes reliant on dendritic sodium channels and *N*-methyl-D-asparate receptors. To ensure that our results were not artifacts of narrow parametric choices, we confirmed our results with independent multi-parametric stochastic search algorithms spanning thousands of unique models for each synaptic localization scenario. Through the use of virtual knockout models on the intrinsically heterogeneous model population employed here, we demonstrate a vital role for dendritically expressed voltage-gated ion channels, especially the transient potassium channels, in maintaining sharpness of place-cell tuning. Finally, we also quantitatively demonstrate that synaptic potentiation targeted to afferents from one specific place field to be sufficient to enforce place-field selectivity, even when intrinsically disparate neurons received randomly dispersed afferents from multiple place-field locations.

Our results provide clear lines of quantitative evidence that spatial clustering of synapses is neither essential for the generation of dendritic spikes nor a requirement for sharp tuning of neuronal responses to input features. We argue that this ability of neurons to achieve nonlinear input processing and sharp feature selectivity with randomly dispersed iso-feature synapses equips them with significant degrees of freedom towards achieving sharp tuning. These quantitative lines of evidence also dispel the impression

4

that dispersed and clustered synaptic localization strategies exclusively translate to linear and nonlinear modes of dendritic operation, respectively. Together, we postulate that there are distinct advantages for the dispersed localization strategy especially for spatial tuning in the adult hippocampus where new place cells are routinely formed in an experience-dependent manner.

RESULTS

As a first step in addressing questions on the impact of channel and synaptic localization profiles on sharpness of place-cell tuning profiles, we employed a morphologically realistic conductance-based model of a CA1 pyramidal neuron with channel distributions and physiological measurements (Fig. 1*A–G*) that matched their electrophysiological counterparts (Magee and Johnston, 1995; Spruston et al., 1995; Hoffman et al., 1997; Magee, 1998; Narayanan and Johnston, 2007, 2008, 2012; Rathour and Narayanan, 2014). To match with corresponding experimental observations, we scaled receptor conductances such that the unitary EPSP amplitude at the soma was of 0.2 mV amplitude (Fig. 1*H–I*) irrespective of synaptic location across the dendritic arbor (Andrasfalvy and Magee, 2001). In systematically assessing the impact of synaptic localization profiles on place cell tuning, we placed synapses activated by the same place field at different locations across the somatodendritic arbor and computed sharpness of tuning in the neuronal firing rate for each of these localizations.

Models with synapses clustered at the soma elicited sharply-tuned place fields with disparate combinations of channel conductances

As a first step, we placed several (N_{syn}=100 or 500) conductance-based synapses, receiving afferent presynaptic activity as Gaussian-modulated theta waveform (Eq. 13) from the same place field (Geisler et al., 2010), on the soma (Fig. 2*A*). With this afferent synaptic configuration, we found that the base model was capable of eliciting place-cell-like firing responses when N_{syn} was 100, but entered depolarization-induced block when N_{syn} was increased to 500 (Fig. 2*A*). To quantify the sharpness of the neuronal response to

6

the afferent drive, we employed two measurements: the full-width at half maximum (FWHM) and the maximal firing rate (F_{max}) of the neuron's firing rate profile (Fig. 2A).

Was this sharp tuning that was obtained with somatic localization of synapses critically reliant on the specific conductance values set in the hand-tuned base model? Were there explicit constraints on channel conductances to elicit sharply tuned place field responses with somatic localization of synapses? To explore this, we implemented a multi-parametric multi-objective stochastic search (MPMOSS) algorithm (Foster et al., 1993; Goldman et al., 2001; Prinz et al., 2004; Marder and Taylor, 2011; Rathour and Narayanan, 2012b, 2014; Anirudhan and Narayanan, 2015; Mukunda and Narayanan, 2017) on all the five active channel conductances ($\overline{g}_{Na}$, $\overline{g}_{KDR}$, $\overline{g}_{KA}$, $\overline{g}_{h}$ and $\overline{g}_{CaT}$), while scaling their respective gradients with reference to changes in these maximal values (Table 2). We generated 5000 models with each of these maximal conductance values randomly picked from independent uniform distributions spanning 0.5–2 fold of their respective base model values. We activated somatically localized synapses (N_{syn}=100) with stochastic place-field afferent inputs (Eq. 13) to each of these 5000 models, computed the firing rate profile of the action potential response and calculated FWHM and F_{max} for each of these 5000 models.

A representative set of 5 such model responses indicated similar sharp tuning across all these models (Fig. 2B). However, the channel conductances that governed these models exhibited wide-ranging variability (Fig. 2C), implying that sharp place field tuning elicited by somatic localization of place-field synapses was not critically reliant on the specific values of channel conductances. To further confirm this, we plotted the FWHM and F_{max} of all 5000 models, and found minimal variability in these

7

measurements suggesting similar tuning (Fig. 2D). Next, we picked 100 sharply-tuned (low FWHM and high F_{max}) models and asked if there were pairwise correlations between these model parameters. We found weak pairwise correlation coefficients (maximum R=0.652; minimum R=–0.238; mean ± SEM=0.055 ± 0.080) across all conductance values in these sharply-tuned place cell models (Fig. 2E). As all models manifested similar tuning properties, we performed the correlation analysis for all 5000 models, and as expected (Rathour and Narayanan, 2014; Mukunda and Narayanan, 2017), the correlation values grew weaker with increase in the number of models (maximum R=0.007, minimum R=–0.021 with N_{valid}=5000; mean ± SEM=–0.004 ± 0.002). Together, these results demonstrated that with somatic localization of place-field synapses, disparate channel combinations could yield similar tuning profiles with weak pairwise correlations between the underlying channel conductances.

Spatially clustered inputs on one or two oblique dendrites did not confer sharpness in place cell tuning

Motivated by lines of evidence suggesting functional dendritic clustering of similar afferent inputs across different neurons (Takahashi et al., 2012; Winnubst and Lohmann, 2012; DeBello et al., 2014; Druckmann et al., 2014; Wilson et al., 2016), we placed synapses (N_{syn}=100 or 500) with identically stochastic (Eq. 13) activation profiles either on a single oblique or split equally across two distinct obliques. Irrespective of whether synapses were placed on one or two obliques, and irrespective of the number of total synapses, we found that the firing rate was low and the place-field profile flat (Fig. 3), implying weak tuning of the place cell response. Given the critical role of oblique dendritic channel conductances in mediating dendritic spikes (Losonczy and Magee,

8

2006; Losonczy et al., 2008), could this conclusion be an artifact of the specific set of channel conductances in the obliques? To check this, we first performed single sensitivity analysis on each of the several oblique channel conductances by individually varying each of the three subthreshold conductances ($\overline{g}_{CaT}$, $\overline{g}_h$ and $\overline{g}_{KA}$) spanning a large range of 1–141 fold of their base values (Fig. S1). We performed this sensitivity analysis for synaptic localization spanning one or two obliques, with different number of synapses. Irrespective of changes to oblique channel conductances or to the number of synapses, the place cell responses remained weakly tuned for both single/double-oblique localizations (Fig. S1).

We reasoned that these single-sensitivity analyses did not assess the possibility where different combinations of oblique channel conductances evoke sharply tuned place cell responses. For instance, higher densities of regenerative conductances coupled with lower values for restorative conductances could enhance the excitability of these obliques, thereby providing a higher probability of eliciting dendritic spikes. To explore this possibility, we performed two different MPMOSSs spanning all the conductances ($\overline{g}_{CaT}$, $\overline{g}_h$, $\overline{g}_{KA}$, $\overline{g}_{KDR}$ and $\overline{g}_{Na}$; N_{syn}=100) in the one or two obliques, respectively depending on whether synapses were localized onto one (5-parameter MPMOSS; Fig. 4B–D) or two (10-parameter MPMOSS; Fig. 4F–H) obliques. The stochastic search on each conductance spanned 0.5–2 fold of their respective base values. We computed the firing rate profile and calculated FWHM and F_{max} for each of the two sets of 5000 models obtained from the two MPMOSS algorithms.

A representative set of 5 such model responses indicated that the tuning was weak across these models irrespective of whether synapses were localized on one (Fig. 4A) or

9

two (Fig. 4E) obliques although the corresponding channel conductances that governed these models manifested wide-ranging variability (Fig. 4B, Fig. 4F). This implied that the weak place field tuning elicited by synaptic localization on one or two obliques was not critically reliant on the specific values of channel conductances. To further confirm this, we plotted the FWHM and F_{max} of all 5000 models, and found minimal variability in these measurements suggesting similarly weak tuning (Fig. 4C, Fig. 4G). We found weak pairwise correlation coefficients (one oblique: maximum R=0.264; minimum R=–0.104; mean ± SEM=0.009 ± 0.036, N_{valid}=74; two obliques: maximum R=0.365; minimum R=–0.707; mean ± SEM= –0.027 ± 0.03, N_{valid}=46) across all conductance values in the similarly best tuned of these place cell models (Fig. 4D, Fig. 4H). As all models manifested similar tuning properties, we performed the correlation analysis for all 5000 models in each case, and the correlation values grew weaker with increase in the number of models employed to compute the correlation coefficients (one oblique: maximum R=0.007; minimum R=–0.021; mean ± SEM=0.004 ± 0.002, N_{valid}=5000; two obliques: maximum R=0.033; minimum R=–0.034; mean ± SEM=0.0005 ± 0.002, N_{valid}=5000). Together, these results provided ample lines of evidence that spatially clustered inputs confined to one or two dendritic branches were incapable of confer sharpness in place cell tuning, irrespective of the specific values of oblique channel conductances or the number of synapses.

Dispersed synaptic inputs result in sharply tuned place cell responses

As a next step, we randomly distributed the same set of synapses (N_{syn}=100) throughout the proximal apical region (radial distance from soma ≤ 300 μm) of the dendritic tree, with all of them receiving afferent place cell activity identically stochastic (Eq. 13) to

earlier scenarios. There were 399 possible synaptic locations within this proximal apical region with large intersynaptic distances (Fig. S2), which precluded the possibility of incidental clustering of synapses when they were randomly dispersed across these locations. We computed the somatic firing rate response and found F_{max} and FWHM to be comparable to the scenario where synapses were somatically localized, indicative of sharply tuned place cell response (Fig. 5A; *cf.* Fig. 2A). Similar sharp tuning was achieved for different randomizations (within the 300 μm location) of dispersed synaptic localization (Fig. 5A). When we increased the number of synapses to 200, we noted a reduction in spike height, especially at the center of the place field as a consequence of high excitability and inadequate recovery of sodium channels from inactivation. Therefore, we proceeded with N_{syn}=100 (as with earlier localizations).

Was this conclusion on sharp tuning with dispersed synaptic inputs an artifact of the specific choice of channel conductances and their localization profiles in the base model? Is there any specific constraint on channel localization profiles for achieving such sharp tuning of place cell responses with dispersed synaptic inputs? To answer these questions, we performed an MPMOSS on 20 intrinsic parameters (Table 2) with each parameter independently and randomly picked from uniform ranges that spanned 0.5–2 fold of their respective base model values. We selected 90 out of these 5000 GSA models as best-tuned valid models based on similarly low FWHM (<2.5 s) and high F_{max} (> 55 Hz). We found that despite the similarly sharp tuning profiles of five different cells picked from this population of 90 (Fig. 5B), the underlying parametric distributions that defined these models covered the entire span of their respective ranges (Fig. 5C). Finally, we assessed pairwise correlations of the parameters underlying the 90 valid models (Fig.

11

6) and found weak pair-wise correlation across all assessed parameters (maximum R=0.725; minimum R=−0.387, mean ± SEM= 0.012 ± 0.010 , N_{valid}=90). Together, these results (Figs. 5–6) provide clear lines of evidence for multiple realizability of sharply tuned place field responses with dispersed synaptic localization profiles, with different randomized distributions of synapses (Fig. 5A) and with disparate channel localization profiles (Fig. 5–6).

Tuning sharpness and excitatory ramp in somatic voltage response were dependent on the number of synapses

How dependent were our conclusions thus far on the number of synapses? Do these models exhibit an excitatory ramp in their somatic voltages, a characteristic feature in place cell recordings (Harvey et al., 2009; Bittner et al., 2015)? Was this excitatory ramp dependent on the number of synapses employed? Does the somatic voltage trace reflect the theta modulation from the synaptic drive that the neurons receive? Do answers to these questions depend on the specific localization profile of synapses across the somato-dendritic arbor? Would a reduction in number of synapses in the one- and two-oblique localization cases enhance tuning sharpness? To address these questions, we employed valid models from all the three distinct MPMOSS procedures with different synaptic localization profiles (in Figs. 4–5) and computed F_{max} and FWHM of place-cell firing. We found that the peak firing rate and FWHM reduced with reduction in the number of synapses, irrespective of whether the synapses were randomly dispersed (Fig. 7A–C), or were confined within one (Fig. S3A–C) or two (Fig. S3A–C) obliques. Importantly, irrespective of number of synapses associated with a place field, F_{max} was always the largest and the FWHM was always the least with the dispersed synaptic localization

12

strategy compared to the synaptic clustering strategy involving one or two obliques. These observations demonstrated invariance of our conclusion (in Figs. 4–5) — that tuning sharpness achieved with dispersed synaptic localization was better than those achieved with clustering within one or two obliques — to number of activated synapses, and adds further lines of evidence on the effectiveness of dispersed synaptic localization in achieving sharply tuned place cell responses.

Next, we smoothed somatic voltage traces of all valid models (from Figs. 4–5) to eliminate spikes and asked if they exhibited an excitatory ramp that has been observed in place cell recordings. We performed this analysis with models activated with different numbers of synapses, and repeated these analyses for the three different synaptic localization strategies (Fig. 7*D*, Fig. S4*A–B*). Although none of the models with any of the localization strategies elicited action potentials when they were activated with 10 synapses, they exhibited a subthreshold excitatory ramp of a few mV in amplitude (Fig. 7*D*, Fig. S4*A–B*). As the number of activated synapses increased, the amplitude of the excitatory ramps expectedly increased, with much larger ramps achieved with the dispersed localization strategy than with the single- or double-oblique clustering strategy (Fig. 7*D–E*, Fig. S4*A–C*). Additionally, again in a manner reflective of the firing rate profiles obtained with the different localization strategies, the ramps achieved with the dispersed localization strategy were sharper than those with the clustering strategies (Fig. 7*E*, Fig. S4*C*).

Finally, to understand theta modulation of somatic membrane potentials, we smoothed the somatic voltage traces enough to eliminate spikes but to retain theta oscillatory patterns. We performed Fourier analysis on these smoothened traces and

13

found the peak frequency of these spectra (Fig. 7D, Fig. S4A–B). If the somatic traces reflect the synaptic activation profile, they should exhibit an 8 Hz oscillatory pattern (Eq. 13). We found strong ~8-Hz power in most models with dispersed synaptic localization irrespective of number of synapses employed (Fig. 7D, Fig. 7F), suggesting that the temporal precision within the theta range was not lost with dispersed synaptic localization However, when synapses were clustered within one or two obliques, we found several models where 8 Hz was not the dominant frequency in these smoothed voltage traces, especially when the number of synapses were higher (Fig. S4A–B, Fig. S4D). This implied a loss of temporal precision in the theta range when large number of synapses were confined within one or two obliques. Together, these results suggested significant advantages for dispersed synaptic localization, equipped with a sharper firing profile, a sharper excitatory ramp and temporally precise transfer of synaptic inputs in the theta range. With clustered synaptic localization confined only to one or two obliques, on the other hand, the firing rate tuning and the ramp were broader with much lower firing frequencies irrespective of the number of synapses employed.

Dispersed synaptic localization was sufficient to elicit dendritic spikes

What biophysical mechanisms were responsible for the sharp tuning of place cell responses in models with dispersed synaptic localization? Why did synaptic localization confined to one or two obliques not yield sharp tuning? Motivated by the evidence for the role of dendritic spikes in sharp tuning of place cells (Sheffield and Dombeck, 2015), we simultaneously recorded voltage traces at various points along the somatoapical arbor corresponding to each somatic action potential. We performed these recordings for the four different synaptic localization profiles and analyzed these traces specifically for

14

signatures of dendritic spikes (Fig. 8). Specifically, whereas a backpropagating action potential (bAP) would manifest as a dendritic voltage peak *following* the somatic action potential peak, a dendritic spike that potentially participated in the emergence of the somatic action potential would express as a dendritic voltage peak that *precedes* the somatic action potential peak.

For the case where the synapses were clustered at the soma (Fig. 2), as expected, all dendritic voltages recorded in conjunction with a somatic action potential were attenuating back propagating action potentials, bAPs (Fig. 8*A*). We confirmed this across all action potentials from all valid models by noting that the latency of bAPs increased with increasing distance from the soma and that there were no dendritic voltages that preceded the somatic action potential across the dendritic arbor (Fig. 8*E–F*). Thus, with this physiologically unrealistic localization profile where there were no synapses in the dendrites, it was possible to achieve sharply tuned profiles of spatial tuning even in the absence of dendritic spikes.

We observed two distinct scenarios when synaptic localization was confined to one oblique. First, during the initial part of the place field when the number of activated synapses was low because of the low probablity of afferent activation (Eq. 13), there were dendritic spikes that were initiated in the oblique where the localization was confined to. However, consistent with *in vitro* lines of evidence (Losonczy and Magee, 2006; Losonczy et al., 2008), these oblique dendritic spikes did not propagate through the trunk to result in a full-blown somatic action potential (Fig. 8*B*). Second, with progressive increase in activation probability of synapses, the afferent excitation was large enough to drive the oblique to depolarization-induced block. This depolarization

15

traversed through the dendritic arbor to elicit somatic action potentials, which backpropagated into the dendrites as bAPs (Fig. 8B). As somatic firing was elicited by the depolarization, and not by precisely timed dendritic spikes or synaptic potentials, the firing frequency was flat across the entire place field (Fig. 8B, Fig. 3–4, Fig. S1). Thus, when synapses were localized to one oblique, the afferent synaptic drive either elicited local dendritic spikes that did not result in somatic APs or manifested as a large depolarization in the oblique that yielded somatic APs that were weakly tuned. We confirmed this by analyzing all action potentials from all valid models, and noted that there were no dendritic voltages that preceded the somatic action potential across the dendritic arbor (Fig. 8E–F).

Although the overall scenario was pretty similar to the one-oblique case when synapses were localized on two obliques, there were cases where the dendritic voltage peak preceded the somatic action potential peak (Fig. 8C, Fig. 8E–F). As these dendritic spikes were not distinctly observed in the two obliques where the synapses impinged and were observed on the trunk, we reasoned that the combined depolarization imposed on the trunk by the two obliques was sufficient to elicit dendritic spikes on the trunk. These dendritic spikes then propagated to the soma to elicit full-blown action potentials. However, the large depolarization-induced block introduced in both obliques and the consequent flat somatic firing rate profile implied that the tuning was weak when synapses were localized to two obliques (Fig. 8C, Fig. 3–4, Fig. S1).

Could the depolarization-induced block observed with single and double oblique localization profiles be because the synaptic drive was large? Would these models elicit sharply tuned profiles driven by localized dendritic spikes if the number of synapses were

16

reduced? To address these, we analyzed the somatodendritic voltage traces from single- and double-oblique models with lesser numbers of synapses. As mentioned earlier, reducing the number of synapses did not yield sharp tuning (Fig. S3) either with single or double oblique synaptic localization. Closer assessment of the somatodendritic voltage traces obtained with different synapses confirmed our previous conclusions obtained with 100 synapses. Specifically, when the number of synapses were lower, the oblique dendrites where synapses were placed showed dendritic spikes which did not propagate to the cell body (Fig. S5*A–C*). When we gradually increased the number of synapses, the voltage profile within the oblique exhibited depolarization-induced block, and this depolarization travelled to the soma to elicited weakly tuned spatial firing with lesser temporal precision in the theta range (Fig. S5*A–C*, Fig. S4). Together (Fig. 8*A–B*, Figs. S3–S5), functional clustering on one or two oblique dendrites either generated localized dendritic spikes that did not propagate to result in a somatic AP or resulted in a large depolarizing drive that flattened the firing rate at the soma thereby yielding weakly tuned place field responses.

Strikingly, dendritic spikes preceding somatic action potentials were more prevalent (compared to all other synaptic localization profiles) in the scenario where synapses were dispersed across the dendritic arbor (Fig. 8*D–F*). These results demonstrated that widespread depolarization coupled with large-amplitude local EPSPs resulting from the high synaptic strengths (Fig. 1*G*) was sufficient to elicit precisely timed dendritic spikes that together resulted in sharply tuned place field responses. Importantly, these results provide clear lines of quantitative evidence that spatial

17

clustering of synapses is neither essential for the generation of dendritic spikes nor a requirement for sharp tuning of place field responses.

When we plotted action potential/dSpike amplitude as a function of distance, we found an expected reduction with distance (Fig. 8*G*). However, the amplitude of bAPs with somatic localization of synapses was lower compared to all the other synaptic localization profiles. As EPSP-driven direct dendritic depolarization was the major difference between somatic and other localization scenarios, we reasoned the higher bAP/dSpike amplitude obtained with the three other synaptic localizations to be consequent to the inactivation of *A*-type K^+ channels by the afferent depolarization (Hoffman et al., 1997; Magee and Johnston, 1997; Watanabe et al., 2002; Frick et al., 2004).

Dendritic sodium channels and synaptic NMDARs were essential to the emergence of sharp place cell responses when synaptic localization was dispersed

We next asked if apical dendritic sodium channels and NMDARs were essential for the sharp tuning of place cell responses when synapses were dispersed. In doing this, we employed the virtual knockout model (VKM) technique (Rathour and Narayanan, 2014; Anirudhan and Narayanan, 2015; Mukunda and Narayanan, 2017) on each of the 87/90 valid models from the MPMOSS algorithm executed with dispersed synapses (Fig. 6), separately targeting apical dendritic sodium channels and NMDARs. Specifically, we set the apical dendritic NaF conductance or NMDAR permeability in each of these valid models to zero and recorded model responses when identical (to the corresponding valid model) synaptic drive was afferent onto these models. We then compared the voltage traces and firing rate profiles of these knockout models with their respective baselines to

18

assess the role of each component on tuning profiles and dendritic nonlinearities. We found that the absence of dendritic NaF channels or synaptic NMDARs resulted in a significant loss of tuning sharpness in these models (Fig. 9). As expected, knocking out apical dendritic sodium channels resulted in a scenario where there were no dendritic spikes and the action potentials did not spread significantly into the dendritic tree. Although dendritic spikes were prevalent even in the absence of NMDARs because dendritic NaFs were still present, the tuning sharpness was significantly reduced and the fraction of dendritic spikes were also lower (Fig. 9). These results suggest dendritic Na channels and NMDARs as essential ingredients in achieving sharp tuning with dispersed synaptic inputs.

Virtual knockout models unveiled a critical role for *A*-type K$^+$ channels in the emergence of sharp place cell tuning

How sensitive was the sharpness of place cell tuning in valid models with dispersed synaptic localization to each ion channel expressed across the neuronal arbor? To address this, we employed the VKM technique to measure place cell profiles in each of the 90 valid models by individually knocking out each of the 3 different subthreshold active conductances (independently setting $\overline{g}_{CaT}$, $\overline{g}_h$ or $\overline{g}_{KA}$ to 0). Although the impact of knocking out these different channels was differential across different models, knocking out the *A*-type K$^+$ channel yielded the maximum reduction in the sharpness of the place cell tuning (Fig. 10). As expected, knocking out the HCN conductance resulted in a slight increase in excitability, whereas on knocking out the CaT conductance there was a slight decrease in excitability (Fig. 10). Together, these results demonstrated a critical role that

19

dendritic ion channels, especially the transient potassium channels, play in maintaining the sharpness of place cell tuning.

Targeted synaptic plasticity was sufficient to provide selective tuning to a single place field in neurons receiving randomly dispersed inputs from several place fields

If individual place fields projected to independent dendritic branches, clustered plasticity as a mechanism could enable enhancement of synapses only on one of these branches, thereby converting a silent cell (that receives input from several place fields) to a place cell that responds only to one specific location (Losonczy et al., 2008; Kleindienst et al., 2011; Magee, 2011; Makino and Malinow, 2011; Lee et al., 2012; Bittner et al., 2015). However, if the synapses are dispersed as postulated here, then synapses corresponding to a given place field will be distributed all across the dendritic arbor, and would have to undergo simultaneous plasticity to convert a silent cell to a place cell. It is feasible to envisage such a scenario because the induction of synaptic potentiation involves *temporal coincidence* of afferent synaptic activation and a postsynaptic depolarization (Magee and Johnston, 1997; Sjostrom et al., 2008) without any specific requirement for spatial clustering. Nevertheless, could sharply tuned selectivity to one place field be achieved in neurons that receive afferent inputs from multiple place fields, each of which are randomly dispersed within the dendritic arbor, and are peri-threshold in terms of their ability to elicit place cell responses? Would the overlaps in the spatial locations of synapses from different place fields, and their interactions with the underlying intrinsic somatodendritic properties preclude such selectivity even when synaptic plasticity is targeted only to synapses from one place field?

20

To address these questions, we independently and randomly dispersed synapses (50 synapses each) from five contiguous place-field locations (total 250 synapses) across the apical dendritic arbor. We had all these place-field inputs to be peri-threshold in the base model, making the model to be a silent cell (Lee et al., 2012; Bittner et al., 2015) by default. The relative distance-dependent gradients of receptor permeabilities (Fig. 1*H*) were maintained in scaling these synaptic permeabilities to achieve peri-threshold excitability from all place fields. With this configuration set as the base model, we employed the MPMOSS framework for a stochastic search on 21 model parameters. The parameters encompassed all the 20 intrinsic parameters (Table 2) and an additional parameter that we referred to as *permfold*, which governed potentiation of synapses associated with only one of the five place field afferents. Specifically, whereas the permeability values for synapses of the chosen place field could randomly vary 1–5 fold (the value of *permfold*) of their respective baseline perithreshold values, the permeabilities for synapses from the other place fields remained at their baseline perithreshold values.

We executed the MPMOSS algorithm to generate 2500 models, each with disparate intrinsic properties and with randomized synaptic potentiation targeted at only one (arbitrarily chosen to be the second place field) of the five place fields. To select valid models in this case, as a first step, we rejected models that either showed no firing or place-nonspecific firing. We accepted only those models that exhibited selective firing only for the chosen place-field (Fig. 11*A*). Quantitatively, we computed the ratio between maximal firing rates of the other place fields and of the chosen place field, and discarded any model that had a ratio beyond 0.1 (10-fold difference between in-field and out-of-

21

field firing rates). Next, from this set of models that preferentially fired for only the second place field, and we selected models that had high F_{max} and low FWHM to obtain 60 valid models.

We chose five of these valid models that exhibited similar sharp tuning to the selected place fields and assessed the parametric distributions with reference to the intrinsic properties and the synaptic permeability of these functionally similar models (Fig. 11*A*). We found significant variability in all model parameters which suggested a lack of constraints on the any of the parameters to elicit the requisite combination of place-field selectivity and tuning sharpness (Fig. 11*B–C*). With reference to the level of synaptic potentiation required, we found a 3–5 fold change in most models that achieved selectivity to the chosen place field (Fig. 11*C*). Finally, we did not observe any substantial pairwise correlation among the parameters, suggesting the expression of degeneracy in intrinsic parameters towards achieving place-field selectivity through targeted synaptic potentiation. Together, these results suggest that variable levels of targeted synaptic potentiation, in conjunction with disparate sets of intrinsic properties, was sufficient to provide sharp and selective place-field tuning in a cell that received randomly dispersed inputs from several place fields.

DISCUSSION

The prime conclusion of this study is that randomly dispersed iso-place-field synaptic localization covering a wide span of dendritic arbor is sufficient to elicit dendritic spikes and sharply tuned place-field selectivity in neuronal responses. We demonstrated this sufficiency with only a small proportion (N_{syn}=50–100) of synapses than those that typically impinge (15,000–30,000) on a pyramidal neuron (Bezaire and Soltesz, 2013), with each synapse physiologically constrained (Andrasfalvy and Magee, 2001) in terms of its unitary somatic EPSP. Employing MPMOSS, we demonstrated this sufficiency for different randomizations of dispersed synaptic localization and of disparate channel conductances. The dendritic spikes and the sharp tuning were critically dependent on dendritic sodium channels synaptic NMDA receptors and A-type K$^+$ channels, providing clear lines of quantitative evidence for a nonlinear mode of neuronal processing despite the dispersion in synaptic localization. Finally, we demonstrated that despite randomly dispersed localization of synapses from several place field afferents, targeted synaptic potentiation was capable of eliciting sharp and selective tuning to one specific place field.

Synaptic localization strategies and plasticity towards place cell formation

It is evident from our analyses here that the prevalent dogma on the exclusiveness of linear *vs.* nonlinear modes of operation occuring respectively with dispersed *vs.* clustered synaptic localization ignored several features of hippocampal pyramidal neurons. First, the high density AMPARs in dendritic locations implies a large local dendritic voltage deflection corresponding to their afferent activation (Andrasfalvy and Magee, 2001). Second, the opening of slowly-decaying, voltage-dependent NMDARs (Jahr and Stevens, 1990) following this large voltage deflection mediated by AMPARs manifests as a wider

23

spread of a nonlinearly amplified depolarization (Schiller and Schiller, 2001; Branco et al., 2010) given that slower signals traverse longer and provide the substrate for better temporal summation (Rall, 1977). Third, given the extents of spatial influence of ion channels and given interactions among depolarizations from multiple dispersed synapses (Branco et al., 2010; Rathour and Narayanan, 2012a), the combined large depolarizations emerging from the two receptor subtypes on each synapse was sufficient to cross the threshold for generating dendritic spikes (Fig. 8). Finally, converging depolarizations and propagating dendritic spikes from several concomitantly-active dispersed synapses was sufficient to elicit temporally precise somatic action potentials yielding sharply tuned neuronal responses (Fig. 5–9).

Whereas these observations yield insights into the scenario where dispersed synaptic inputs yielded dendritic spikes and sharply tuned neuronal responses, our analyses also make a case for why synapses clustered on one or two obliques wouldn't yield sharp tuning despite resulting in dendritic spikes in certain cases. First, it is well established that propagation of single oblique dendritic spikes, resulting from spatiotemporally clustered synaptic activation, to yield full-blown somatic action potentials is weak, differential and state-dependent (Golding and Spruston, 1998; Gasparini and Magee, 2006; Losonczy and Magee, 2006; Losonczy et al., 2008; Sjostrom et al., 2008). The reasoning behind the link between clustered synaptic activation and sharp tuning of neuronal responses is that spatial and temporal summation of multiple such oblique spikes manifests as sharply tuned neuronal firing responses. However, the case for temporal summation of dendritic spikes from *within* a single oblique is weakened by the presence of dendritic sodium channels whose recovery from inactivation is very

24

slow (Colbert et al., 1997). Such slow recovery from inactivation argues against fast repetitive generation of dendritic spikes in a single oblique, instead converting large afferent drives into depolarization-induced block (Fig. 4, Fig. 8, Fig. S5). Together, these translate into one of two alternatives when synapses (irrespective of their numbers) are clustered on one or two obliques: a non-propagating oblique spike or a weakly-tuned somatic response consequent to the depolarization traveling from the oblique (Fig. 8, Fig. S5).

In our analyses, we tested synaptic localization profiles confined to one or two oblique dendrites. However, the localization strategies form a continuum from the single oblique cluster to the randomized dispersion ends. Therefore, it is easy to extrapolate the possibility of attaining sharply tuned neural responses with the same number of synapses localized to multiple (not just one or two) obliques. This, in turn, points to two distinct somatodendritic synaptic localization strategies towards achieving sharply tuned firing responses through generation and propagation of dendritic spikes: random dispersion of synapses *vs.* specifically clustered localization limited to a few obliques for each perceptual feature.

Although either strategy would yield sharply tuned responses and it is possible that different neurons employ different strategies, we postulate that there are distinct advantages in choosing the dispersed localization strategy *especially* in the adult hippocampus where new place cells are routinely formed in an activity-dependent manner. First, the rewiring and synapse-formation requirements for targeting afferent synapses corresponding to a newly-forming place field specifically onto a few obliques are more demanding than dispersing these synapses randomly across the dendritic arbor.

25

Second, recent evidence indicates that synapses corresponding to different place fields impinge on silent cells (Lee et al., 2012; Bittner et al., 2015; Domnisoru and Tank, 2016). The presence of synapses from several place fields on a single neuron poses a resource allocation problem with reference to specific neuronal surface area assigned to each of these synaptic subsets (each corresponding to different place fields). The randomized dispersed localization scenario provides a better solution to the allocation problem rather that assigning multiple of the limited number of obliques to each of these different place fields, especially when the number of place fields to be allocated becomes large. This is possible because of the ability of the neuron to achieve robust tuning with different randomizations of dispersed synaptic profiles (Fig. 5) and with disparate channel conductances (Fig. 6). This enormously increases the degrees of freedom available for achieving sharp place cell tuning with randomly dispersed synaptic localization.

Finally, from a plasticity perspective, the solution involving clusters on multiple obliques seems to offer a distinct advantage given the several demonstrations of clustered synaptic plasticity (Govindarajan et al., 2011; Makino and Malinow, 2011). However, plasticity involves *temporal coincidence* of afferent synaptic activation and a postsynaptic depolarization (Magee and Johnston, 1997; Sjostrom et al., 2008), say a widespread plateau potential that even invades the soma (Bittner et al., 2015). Importantly, our results offer direct quantitative evidence for the ability of targeted synaptic potentiation to achieve sharp selectivity to one place field even when multiple place field afferents impinge onto a neuron in a dispersed manner (Fig. 11). Our results also demonstrate degeneracy, whereby such sharp selectivity could be achieved in cells with significantly disparate channel properties and with variable levels of synaptic

potentiation. These observations allow for more degrees of freedom for plasticity driven by temporal coincidence of afferent inputs with a postsynaptic depolarization to achieve place-field selectivity. Together, our results provide quantitative evidence that spatial dispersion of synapses is unlikely to be an impediment for localized plasticity in synaptic receptors and/or synapse-adjacent ion channels (Frick et al., 2004; Losonczy et al., 2008; Sjostrom et al., 2008) towards the formation of novel place cells with dispersed synaptic localization. Our observations offer an advantageous clear alternative to synaptic clustering in achieving sharp feature selectivity through dendritic spike initiation with randomly dispersed iso-feature synaptic afferents.

Limitations and future directions

Although our model was severely constrained for electrophysiological details from hippocampal pyramidal neurons, the model bears limitations in terms of other factors that could alter place-cell tuning. First, as our focus is on localization and spatiotemporal summation of excitatory synaptic inputs, we did not incorporate inhibition into our model. However, inhibitory synapses play a critical role in the generation and propagation of dendritic spikes (Milstein et al., 2015; Grienberger et al., 2017). Second, absent in our model are several membrane and subcellular components, such as calcium stores on the endoplasmic reticulum, metabotropic receptors for different neurotrasmitters and neuromodulators, other channels such as the calcium-activated potassium, G-protein coupled and store-operated calcium, and well-established cross interactions among those components and channels/receptors included in our model (Ashhad and Narayanan, 2013; Grienberger et al., 2015). Third, activation of synapses carrying place field information could lead to gliotransmision or release of retrograde messengers from the pyramidal

27

neuron that could affect the dendritic and network integration processes (Regehr et al., 2009; Araque et al., 2014; Ashhad and Narayanan, 2016). These limitations and missing components make a critical case for their incorporation into future models with different synaptic (including inhibitory and neuromodulatory synapses) localization profiles, including their short-term synaptic dynamics (Regehr, 2012). However, the several electrophysiological constraints we had imposed on our model and the conclusions from our broad array of sensitivity analyses are fairly strong to postulate the validity of our conclusions even when these other components are considered. Additionally, although our conclusions are largely extendible to pyramidal neurons in other brain regions, the specifics of morphological characteristics, passive properties, ion channels and receptors expressed there should be rigorously assessed before formulating such an extrapolation.

MODELS AND METHODS

A morphologically realistic reconstruction of a CA1 neuron (*n123*) was obtained from the NeuroMorpho database (Pyapali et al., 1998; Ascoli et al., 2007), and passive and active properties for the base model were adopted from an earlier model (Rathour and Narayanan, 2014) that matched several somatodendritic functional maps (Narayanan and Johnston, 2012) through physiologically established channel localization profiles (Fig. 1*A–G*). The specific membrane capacitance was set uniformly at 1 μF/cm^2. R_m and R_a were set in a gradient along the trunk as a function of the radial distance of the compartment from the soma according to the equations and parametric values in Tables 1–2 (Fig. 1*B*). The basal dendrites and the axonal compartments had somatic R_m and R_a, and the apical obliques had the same R_m and R_a as the trunk compartment from which they originated. The model was compartmentalized according to the d_λ rule (Carnevale and Hines, 2006) to ensure isopotentiality in each compartment. Specifically, each compartment was smaller than $0.1 \times \lambda_{100}$, with λ_{100} representing the space constant of the section computed at 100 Hz. The five different ion channels used in the model were Hodgkin-Huxley-type delayed rectifier potassium (KDR), fast sodium (NaF), *T*-type calcium (CaT), hyperpolarization-activated cyclic-nucleotide-gated (HCN) nonspecific cation and *A*-type potassium (KA) channels (Table 1). Currents through the NaF, KDR, KA and HCN channels employed an Ohmic formulation with reversal potentials for Na$^+$, K$^+$ and *h* channels set at 55, –90 and –30 mV respectively. The CaT current was modeled using the Goldman-Hodgkin-Katz (GHK) convention (Shah et al., 2008).

NaF and KDR conductances were distributed uniformly in the soma and across the dendritic arbor with respective maximal conductances set at $\overline{g}_{Na}$ = 16 mS/cm^2 and

$\overline{g}_{\mathrm{KDR}}$ = 10 mS/cm^2 (Magee and Johnston, 1995; Hoffman et al., 1997). The $\overline{g}_{\mathrm{Na}}$ in the axonal initial segment was five times higher compared to the somatic value. The rest of the axon was considered to be passive. As the recovery of dendritic sodium channels from inactivation is slower (Colbert et al., 1997), an additional inactivation gating variable was included in the model for Na$^+$ channels that expressed in the apical dendrites (Migliore et al., 1999). The three subthreshold channel conductances (CaT, HCN and KA) were distributed with increasing somato-apical gradients (Table 1, Fig. 1B), dictated by corresponding electrophysiological findings (Magee and Johnston, 1995; Hoffman et al., 1997; Magee, 1998). In incorporating electrophysiological observations on differences between the activation parameters of the KA channels in CA1 pyramidal cells (Hoffman et al., 1997), two different KA conductance models were employed for proximal (≤100 μm radial distance from soma) and distal (>100 μm) apical dendritic compartments (Migliore et al., 1999). The half-maximal activation voltage for HCN channels was –82 mV for proximal apical compartments (radial distance ≤ 100 μm), linearly varied from –82 mV to –90 mV for compartments between 100 and 300 μm, and was set at –90 mV for compartments with distances larger than 300 μm (Magee, 1998). All active and passive properties of basal dendritic compartments were set to their respective somatic values.

All somatodendritic active and passive parameters and their gradients were tuned to match distance-dependent electrophysiological measurements (Fig. 1C–G) of back-propagating action potentials (bAP), input resistance (R_{in}), resonance frequency (f_{R}) and total inductive phase (Φ_{L}) from CA1 pyramidal neurons (Spruston et al., 1995; Hoffman et al., 1997; Narayanan and Johnston, 2007, 2008; Rathour and Narayanan, 2014).

Intrinsic measurements

All intrinsic measurements (bAP, R_{in}, f_R and Φ_L) were computed using procedures described earlier (Spruston et al., 1995; Hoffman et al., 1997; Narayanan and Johnston, 2007, 2008; Rathour and Narayanan, 2014). Briefly, to measure dendritic bAP, an action potential was initiated at the soma (2 nA current for 1 ms) and the bAP amplitude was measured at various locations along the somatoapical trunk (Fig. 1*C*). R_{in} was measured by injecting subthreshold current pulses of amplitudes spanning −50 pA to +50 pA, in steps of 10 pA and recording the local voltage responses to these current pulses. The respective steady state voltage responses at a given location were plotted against the corresponding current amplitudes to obtain the *V-I* plot. The slope of a linear fit to this steady-state *V-I* plot was taken as the R_{in} for that location, and the procedure was repeated for all locations along the somatoapical trunk (Fig. 1*D*).

Impedance-based measurements of the model were computed by injecting a chirp stimulus (Narayanan and Johnston, 2007, 2008; Rathour and Narayanan, 2012b, 2014): a sinusoidal current wave with constant amplitude (100 pA; peak-to-peak) with frequency linearly increasing from 0.1 to 15 Hz in 15 s (Fig. 1*E*, top). The Fourier transform of the local voltage response (Fig. 1*E*, bottom) was divided by the Fourier transform of the chirp stimulus (Fig. 1*E*, top) to obtain the complex valued impedance $Z(f)$, as a function of frequency f. The impedance amplitude profile $|Z(f)|$ was computed as the magnitude of this impedance:

$$\left| Z(f) \right| = \sqrt{\left(\mathrm{Re}(Z(f)) \right)^2 + \left(\mathrm{Im}(Z(f)) \right)^2} \qquad (1)$$

where $\mathrm{Re}(Z(f))$ and $\mathrm{Im}(Z(f))$ were the real and imaginary parts of the impedance $|Z(f)|$, respectively. The frequency at which $|Z(f)|$ reached its maximum value was measured as

the resonance frequency, f_R, and was computed at each location along the somatoapical trunk (Fig. 1F). The impedance phase profile $\phi(f)$ was computed as:

$$\phi(f) = \tan^{-1}\frac{\text{Im}(Z(f))}{\text{Re}(Z(f))} \tag{2}$$

Φ_L, defined as the area under the inductive part of $\phi(f)$, (Narayanan and Johnston, 2008), was computed for all locations along the somato-apical trunk (Fig. 1G) based on the local impedance phase profile:

$$\Phi_L = \int\limits_{\phi(f)>0} \phi(f) df \tag{3}$$

Synaptic models and normalization of unitary potentials

Canonical synapses (default #synapses: 100) consisting of co-localized N-Methyl-D-Aspartate (NMDA) and α-amino-3-hydroxy-5-methyl-4-isoxazolepropionic acid (AMPA) receptors were modeled using the GHK convention, with the default value of NMDAR:AMPAR ratio set at 1.5. The kinetics of AMPA and NMDA receptor currents were adopted from previous literature (Narayanan and Johnston, 2010; Ashhad and Narayanan, 2013; Anirudhan and Narayanan, 2015). The current through the NMDA receptor, as a function of voltage and time, was dependent on three ions: sodium, potassium and calcium. Consequently, as per the Goldman-Hodgkin-Katz convention:

$$I_{NMDA}(v,t) = I_{NMDA}^{Na}(v,t) + I_{NMDA}^{K}(v,t) + I_{NMDA}^{Ca}(v,t) \tag{4}$$

where,

$$I_{NMDA}^{Na}(v,t) = \overline{P}_{NMDAR} \, P_{Na} \, s(t) \, MgB(v) \, \frac{vF^2}{RT}\left(\frac{[Na]_i - [Na]_o \exp\left(-\frac{vF}{RT}\right)}{1 - \exp\left(-\frac{vF}{RT}\right)}\right) \tag{5}$$

$$I_{NMDA}^{K}(v,t) = \overline{P}_{NMDAR} \, P_{K} \, s(t) \, MgB(v) \, \frac{vF^2}{RT}\left(\frac{[K]_i - [K]_o \exp\left(-\frac{vF}{RT}\right)}{1 - \exp\left(-\frac{vF}{RT}\right)}\right) \tag{6}$$

$$I_{NMDA}^{Ca}(v,t) = \overline{P}_{NMDAR}\, P_{Ca}\, s(t)\, MgB(v)\, \frac{4vF^2}{RT}\left(\frac{[Ca]_i - [Ca]_o \exp\left(-\frac{2vF}{RT}\right)}{1 - \exp\left(-\frac{2vF}{RT}\right)}\right) \tag{7}$$

where $\overline{P}_{NMDAR}$ is the maximum permeability of the NMDA receptor. The relative permeability ratios were set at P_{Ca}=10.6, P_{Na} =1, P_K =1. Default values of concentrations were (in mM): $[Na]_i$=18, $[Na]_o$=140, $[K]_i$=140, $[K]_o$=5, $[Ca]_i$=100 × 10^{-6}, $[Ca]_o$=2. $MgB(v)$ governs the magnesium dependence of the NMDAR current, given as (Jahr and Stevens, 1990):

$$MgB(v) = \left(1 + \frac{[Mg]_o \exp(-0.062v)}{3.57}\right)^{-1} \tag{S8}$$

with the default value of $[Mg]_o$ set at 2 mM. $s(t)$ governs the kinetics of the NMDAR current, and is given as:

$$s(t) = a\left(\exp\left(-\frac{t}{\tau_d}\right) - \exp\left(-\frac{t}{\tau_r}\right)\right) \tag{9}$$

where a is a normalization constant, making sure that $0 \le s(t) \le 1$, τ_d is the decay time constant, τ_r is rise time, with τ_r =5 ms, and default τ_d =50 ms (Narayanan and Johnston, 2010; Ashhad and Narayanan, 2013).

Current through the AMPA receptor was modeled as the sum of currents carried by sodium and potassium ions:

$$I_{AMPA}(v,t) = I_{AMPA}^{Na}(v,t) + I_{AMPA}^{K}(v,t) \tag{10}$$

where,

$$I_{AMPA}^{Na}(v,t) = \overline{P}_{AMPAR}\, P_{Na}\, s(t)\, \frac{vF^2}{RT}\left(\frac{[Na]_i - [Na]_o \exp\left(-\frac{vF}{RT}\right)}{1 - \exp\left(-\frac{vF}{RT}\right)}\right) \tag{11}$$

$$I_{AMPA}^{K}(v,t) = \overline{P}_{AMPAR}\, P_K\, s(t)\, \frac{vF^2}{RT}\left(\frac{[K]_i - [K]_o \exp\left(-\frac{vF}{RT}\right)}{1 - \exp\left(-\frac{vF}{RT}\right)}\right) \tag{12}$$

33

where $\overline{P}_{AMPAR}$ is the maximum permeability of the AMPA receptor. The relative permeability ratios P_{Na} and P_K were equal and set to 1. $s(t)$ was the same as that for the NMDA receptor, but with τ_r=2 ms and τ_d=10 ms (Narayanan and Johnston, 2010). AMPAR permeabilities for synapses at any somato-apical location (Fig. 1*H*) were adjusted such that the unitary response amplitude was ~0.2 mV (Fig. 1*I*) irrespective of synaptic location (Andrasfalvy and Magee, 2001). This ensured that attenuation along the dendritic cable did not play a critical role in determining the impact of synaptic localization profiles on tuning properties.

Place cell inputs and firing rate measurements

Place-cell inputs were fed as probabilistic afferent activity impinging on the colocalized AMPAR-NMDAR synapses described above. The frequency of place-cell inputs to these synapses were modeled as an excitatory Gaussian modulated cosinusoidal current input driven through conductance-based synapses, with the frequency of the sinusoid set at 8 Hz. This *conductance*-based formulation was modified from (Geisler et al., 2010), where place-cell inputs were modeled as a Gaussian-modulated cosinusoidal *current*. This modification was essential because a current-based input would not account for the driving-force dependence of synaptic currents or the kinetics/voltage-dependence of individual receptors (Eq. 4–12). Therefore, the total afferent current was modeled to arrive through multiple conductance-based synapses whose presynaptic firing rates were probabilistially driven by a Gaussian-modulated theta-frequency cosinusoid representing the place field afferents. Each synapse in the neuron received inputs whose probability of occurrence at any given time point was defined by (Fig. 2*A*, inset):

34

$$F_{pre}(t) = F_{pre}^{max}\left(1 + \cos\left(2\pi f_0(t-T)\right)\right)\exp\left(-\frac{(t-T)^2}{2\sigma^2}\right) \tag{13}$$

where T (5 s) defined the travel time between place field centers, f_0 represented the cosine wave frequency (8 Hz), F_{pre}^{max} regulated the maximal input firing rate and σ defined the width of the Gaussian and controls the extent of the place field (1 s).

When such afferent activity from place fields (Eq. 13) impinged on synaptic receptors (Eq. 4–12) in models with different synaptic localization profiles (see below), current through these receptors drove post-synaptic action potentials in a manner that was reflective of these place-field inputs (*e.g.*, Fig. 2*A*). These spikes were converted to instantaneous firing rate profiles through convolution with a Gaussian kernel. Several measurements were derived from these firing rate profiles (Fig. 2*A*): (a) the maximum firing rate of place cell (F_{max}); (b) the full-width at half maximum (FWHM) of the profile, defined as the temporal distance between the two half-maximal points (on either side of the center) of the profile; (c) area under the curve (AUC) of the firing rate profile. These measurements were employed in comparing different place cell firing profiles, and to define sharpness of the tuning profile. Specifically, a low value of FWHM and a high value of maximal firing rate was considered to be indicative of a sharply tuned place cell response.

Voltage ramps associated with place fields and theta-frequency oscillations in place cell voltage traces

To assess the presence of characteristic ramps that place cells exhibit during place field traversal (Harvey et al., 2009), we subjected model voltage traces obtained during place field traversal (in response to synaptic inputs governed by Eq. 13) to a 0.75 s wide

median filter. This ensured that the spikes were eliminated, thereby revealing the presence or absence of a voltage ramp (*e.g.*, Fig. 7*D–E*). The peak value of the voltage achieved by these ramps were employed as the maximum ramp voltage. Next, although the inputs to the afferent synapses to the neuron were theta-modulated (Eq. 13), the somatic output voltage trace may or may not reflect this theta modulation owing to dendritic filtering or the dominance of afterhyperpolarization conductances. To evaluate theta-modulation in these voltage traces, we subjected model voltage traces obtained during place field traversal to a 50 ms wide median filter. We performed spectral analysis on the resultant waveform and assessed theta modulation of this voltage response by finding the frequency at which the maximum power was observed (*e.g.*, Fig. 7*D*, 7*F*).

Multi-Parametric Multi-Objective Stochastic Search Algorithm

A stochastic search algorithm spanning all critical parameters of the model has been employed as an effective method to (a) test the robustness of the system to parametric variability; (b) find if there are parametric combinations where a specific set of measurement constraints are satisfied; (c) find the relative sensitivities of different measurements to each parameter that forms the system; and (d) explore pair-wise and cross-dependencies across different parameters towards achieving functional homeostasis. In such a global sensitivity analysis approach, each model parameter is assigned a range that spans multiple folds (on either side) of its value in a valid base model that is constrained by physiological measurements from the specific system under consideration. Then, in a given trial, each parameter is independently and randomly chosen through uniform sampling of its respective range to build a model and compute relevant measurements with this chosen set of parameters. Measurements from each of

36

these models are then subjected to a test of validation to examine if they are within their respective physiological bounds. Models that satisfy all the validation criteria are declared as valid models, and parametric combinations that resulted in these valid models could then be analyzed to assess correlations and clustering in valid model parameters. Such parametric analyses, involving valid models that satisfy all functional requirements, provide insights about physiological constraints that need to be placed on model parameters for achieving the given set of functional constraints (Foster et al., 1993; Goldman et al., 2001; Prinz et al., 2004; Marder and Taylor, 2011; Rathour and Narayanan, 2012b, 2014; Anirudhan and Narayanan, 2015; Mukunda and Narayanan, 2017).

As such a stochastic search spans a large space involving multiple physiologically relevant model parameters and validates the resulting stochastic model based on multiple physiological objectives, the percentage of valid models attained through such a procedure is typically low. This translates to a requirement for an exhaustive stochastic search to arrive at a statistically relevant number of valid models. Whereas the presence of valid models provides potential solutions to the multi-objective optimization problem, the absence of any valid model does not necessarily imply infeasibility of such a model configuration towards achieving the physiological objectives. This is simply consequent to the observation that the stochastic search does not *completely* cover the entire *N*-dimensional parametric space, thereby allowing for the possibility where valid solutions could exist within the unexamined regions of the parametric space (Foster et al., 1993; Goldman et al., 2001; Prinz et al., 2004; Marder and Taylor, 2011; Rathour and Narayanan, 2012b, 2014; Anirudhan and Narayanan, 2015; Mukunda and Narayanan,

37

2017). Here we employ such a multi-parametric multi-objective stochastic search (MPMOSS) algorithm to assess the sensitivity of the sharpness of place cell tuning to synaptic and channel localization profiles.

Sensitivity of place-cell tuning to synaptic localization profile

We systematically assessed the impact of placing the same number of afferent synapses with identical impacts on somatic voltages (Fig. 1*I*) with four distinct synaptic localization strategies: (i) all synapses were clustered at the soma (Fig. 2); (ii) all synapses were clustered within a single apical dendritic oblique (Figs. 3–4); (iii) synapses were clustered within two apical dendritic obliques (Figs. 3–4), with both the obliques receiving equal number of synapses; and (iv) synapses were randomly dispersed across the apical dendritic arbor (Fig. 5–6). In all cases, synapses received identical afferent inputs from a given place-field location (Eq. 13), with their permeability adjusted as per their somatodendritic location (Fig. 1*H*) to normalize somatic impact of their activation (Fig. 1*I*). These distinct synaptic localization profiles were systematically tested with different number of synapses (N_{syn}=10, 25, 50, 75, 100, 200 or 500) to analyze the sensitivity of place-cell tuning to the number of synapses in each case (*e.g.*, Fig. 7).

For each of these configurations of the synaptic localization, we employed independent stochastic search strategies on model parameters to assess the sensitivity of the combination of synaptic localization and channel conductances on place cell tuning sharpness. Each stochastic search strategy involved generation of 5000 randomized models spanning different parametric spaces of channel conductances, with each channel conductance assigned a uniform search space of 0.5× to 2× of their respective baseline values (Table 2). As a part of the validation procedure of these stochastically generated

models, we first removed all models that manifested a depolarization-induced block in their voltage output (*e.g.*, Fig. 2*A*, 500 synapses). This was done by plotting a histogram of membrane voltages, and rejecting models that showed a significant peak within the range of –45 mV to 50 mV. Following this, we sorted the models in two ways: first, an ascending order sort of their FWHM and second, a descending order sequence of their maximal firing rate (F_{max}). We selected models that were common to the first part of both the lists, so that they had a similarly small FWHM and a similarly high maximal firing rate, together implying similar sharp tuning of place fields. The distribution of parameters in these selected valid models and their pair-wise correlations were then analyzed to assess the robustness of the system to variability in channel properties and localization (*e.g.,* Figs. 5–6).

Sensitivity of place-cell tuning to channel localization

Whereas channel localization gradients were fixed based on electrophysiological measurements (Fig. 1*B*, Table 1), the dependence of place-cell tuning to individual channel conductances was assessed either through single-channel sensitivity analysis (*e.g.,* Fig. S1) or global sensitivity analysis involving the stochastic search strategy described above. In addition, to assess the specific role of individual channels on different place-cell tuning measurements (FWHM, F_{max} and AUC of the firing rate profile), we performed virtual knockout simulations, where we virtually knocked out each of the different conductances in each valid model obtained through MPMOSS. This was implemented by independently setting the conductance value of each ion channel (performed separately for NMDA receptor permeability and for each of NaF, CaT, KA and HCN channel conductances) to 0 with all the other parameters intact from that

39

specific valid model. Whereas the NaF channel knockout was specific only to apical dendritic compartments (the somatic, AIS and basal dendritic NaF channels were unchanged), all other knockouts spanned the entire somatodendritic arbor. The effect of each knockout was studied by comparing the measurements from the knockout model with respect to the corresponding valid model. This was repeated for all valid models for each knockout, and the statistics of changes in place cell measurements were assessed across the valid model population to gain insights about the role of specific channels in determining place cell tuning profiles (Fig. 9–10).

Dendritic spikes and backpropagating action potentials

To assess the relative timing of spikes at dendritic and somatic locations, we recorded voltage traces at multiple locations along the apical trunk of each valid model obtained from all four MPMOSS algorithms (corresponding to the four synaptic localization strategies) described above. We computed the peak of the spike at several somatodendritic locations for each somatic action potential, detected at the upstroke of the somatic voltage crossing –20 mV. We calculated the differences between the timings of the peak at different dendritic voltages and the timing of the peak somatic voltage. Specifically, for 5 different apical trunk locations (100 μm, 150 μm, 200 μm, 250 μm and 300 μm), we computed the following difference for each somatic spike:

$$\Delta T(sl,nv,tl,sp) = T_{tl}^{peak}(sl,nv,sp) - T_{soma}^{peak}(sl,nv,sp) \qquad (14)$$

where ΔT represented the time difference, sl represented the synaptic localization strategy (somatic, one oblique, two obliques, dispersed), nv indexed the number of valid models $(1, \ldots, N_{valid})$ obtained with the specific synaptic localization strategy, tl represented the five different trunk locations and sp represented the current somatic spike index, and

40

spanned all the somatic spikes obtained for valid model number nv. T_{tl}^{peak} and T_{soma}^{peak} respectively represented the time at which the spike reached its peak at location tl and at the soma. This difference was computed for all spikes in all valid models, and was binned into the appropriate synaptic localization profile sl and location tl.

A dendritic voltage peak occurring before the somatic voltage peak (negative ΔT) was considered to constitute a propagating dendritic spike at the recorded dendritic location, whereas a dendritic peak occurring after the somatic peak (positive ΔT) was representative of a bAP at that location. To quantify the fraction of dendritic spikes that resulted in a somatic action potential, we first plotted the histograms of ΔT for each location tl and each synaptic localization profile sl (Fig. 8E). As negative spike timings represented dendritic spikes occurring before somatic action potentials, we computed the fraction of the total area under the histogram curve that had negative ΔT and assigned that as the fraction of dendritic spikes preceding somatic action potentials. This value was computed for each sl and each tl to compare the impact of synaptic localization on dendritic spike generation (Fig. 8F).

Targeted synaptic plasticity in models receiving multiple place field afferents through randomized dispersed syanpses

We considered temporally sequential inputs from five different place fields, and randomly distributed 50 synapses for each of them (total 250 synapses) on the somato-apical trunk of the CA1 pyramidal cell. With this synaptic configuration, we implemented the MPMOSS algorithm involving all the intrinsic parameters listed in Table 2 and an additional parameter (referred to as permfold, for fold change in permeability) to implement plasticity of synapses that are afferent from one of the five different place

41

fields (arbitrarily chosen to be the second place field). Specifically, by default, the permeability values of all receptors were tuned to be peri-threshold. Then, as part of the MPMOSS strategy, the permeability values of the receptors associated with synapses receiving inputs from the second (of the five) place field were multiplied by a factor (permfold). The value of permfold was part of the stochastic search, and was picked randomly from an uniform distribution spanning 1- to 5-fold of the respective baseline permeability values.

In implementing this MPMOSS strategy, we sampled this 21-parameter search space to search for models and generated 2500 different models. Note that the span of these simulations were 5 times longer than the other simulations, owing to the presence of 5 contiguous place field inputs impinging on the neuron. The goal here was to ask if synaptic plasticity in one set of inputs was sufficient to elicit selectivity to a single place field input when multiple peri-threshold place-field inputs were impinging on the same cell through randomized dispersed synaptic localization (Lee et al., 2012; Bittner et al., 2015). Consequently, the validation criterion here was to assess the selectivity of the neuron to the second placed field (Fig. 11). Specifically, we declared a model to be valid if the peak firing rate of the neuron for inputs arriving from the second place field (in-field firing rate) was at least 10 times the peak firing rate for inputs arriving from any of the other four place fields (out-of-field firing rate). Therefore, neurons that did not fire for any of the different place fields or neurons that fired across all place fields equally would be declared invalid. We chose a MPMOSS strategy that spanned both intrinsic properties and synaptic properties to explore degeneracy in achieving place-field selectivity in scenarios where multiple place fields impinged on the same postsynaptic neuron.

Computational details

All simulations were performed using the NEURON programming environment (Carnevale and Hines, 2006), at 34° C with the resting membrane potential set at –65 mV. The simulation step size was 25 µs. Data analyses and graph plotting were performed using custom-written software in the IGOR Pro environment (Wavemetrics Inc.).

REFERENCES

Andrasfalvy BK, Magee JC (2001) Distance-dependent increase in AMPA receptor number in the dendrites of adult hippocampal CA1 pyramidal neurons. J Neurosci 21:9151-9159.

Anirudhan A, Narayanan R (2015) Analogous synaptic plasticity profiles emerge from disparate channel combinations. J Neurosci 35:4691-4705.

Araque A, Carmignoto G, Haydon PG, Oliet SH, Robitaille R, Volterra A (2014) Gliotransmitters travel in time and space. Neuron 81:728-739.

Ascoli GA, Donohue DE, Halavi M (2007) NeuroMorpho.Org: a central resource for neuronal morphologies. J Neurosci 27:9247-9251.

Ashhad S, Narayanan R (2013) Quantitative interactions between the A-type K+ current and inositol trisphosphate receptors regulate intraneuronal Ca2+ waves and synaptic plasticity. J Physiol 591:1645-1669.

Ashhad S, Narayanan R (2016) Active dendrites regulate the impact of gliotransmission on rat hippocampal pyramidal neurons. Proc Natl Acad Sci U S A 113:E3280-3289.

Bezaire MJ, Soltesz I (2013) Quantitative assessment of CA1 local circuits: knowledge base for interneuron-pyramidal cell connectivity. Hippocampus 23:751-785.

Bittner KC, Grienberger C, Vaidya SP, Milstein AD, Macklin JJ, Suh J, Tonegawa S, Magee JC (2015) Conjunctive input processing drives feature selectivity in hippocampal CA1 neurons. Nat Neurosci 18:1133-1142.

Branco T, Clark BA, Hausser M (2010) Dendritic Discrimination of Temporal Input Sequences in Cortical Neurons. Science 329:1671-1675.

Carnevale NT, Hines ML (2006) The NEURON Book. Cambridge, UK: Cambridge University Press.

Chen X, Leischner U, Rochefort NL, Nelken I, Konnerth A (2011) Functional mapping of single spines in cortical neurons in vivo. Nature 475:501-505.

Colbert CM, Magee JC, Hoffman DA, Johnston D (1997) Slow recovery from inactivation of Na+ channels underlies the activity-dependent attenuation of dendritic action potentials in hippocampal CA1 pyramidal neurons. J Neurosci 17:6512-6521.

DeBello WM, McBride TJ, Nichols GS, Pannoni KE, Sanculi D, Totten DJ (2014) Input clustering and the microscale structure of local circuits. Frontiers in neural circuits 8:112.

Domnisoru C, Tank DW (2016) Monosynaptic inputs to hippocampal place cell dendrites. In: EMBO Workshop on Dendritic Anatomy, Molecules and Function. Foundation for Research and Technology - Hellas (FORTH), Heraklion, Crete.

Druckmann S, Feng L, Lee B, Yook C, Zhao T, Magee JC, Kim J (2014) Structured synaptic connectivity between hippocampal regions. Neuron 81:629-640.

Foster WR, Ungar LH, Schwaber JS (1993) Significance of conductances in Hodgkin-Huxley models. Journal of neurophysiology 70:2502-2518.

Frick A, Magee J, Johnston D (2004) LTP is accompanied by an enhanced local excitability of pyramidal neuron dendrites. Nat Neurosci 7:126-135.

Gasparini S, Magee JC (2006) State-dependent dendritic computation in hippocampal CA1 pyramidal neurons. J Neurosci 26:2088-2100.

Geisler C, Diba K, Pastalkova E, Mizuseki K, Royer S, Buzsaki G (2010) Temporal delays among place cells determine the frequency of population theta oscillations in the hippocampus. Proc Natl Acad Sci U S A 107:7957-7962.

Golding NL, Spruston N (1998) Dendritic sodium spikes are variable triggers of axonal action potentials in hippocampal CA1 pyramidal neurons. Neuron 21:1189-1200.

Goldman MS, Golowasch J, Marder E, Abbott LF (2001) Global structure, robustness, and modulation of neuronal models. J Neurosci 21:5229-5238.

Govindarajan A, Israely I, Huang SY, Tonegawa S (2011) The dendritic branch is the preferred integrative unit for protein synthesis-dependent LTP. Neuron 69:132-146.

Grienberger C, Chen X, Konnerth A (2015) Dendritic function in vivo. Trends Neurosci 38:45-54.

Grienberger C, Milstein AD, Bittner KC, Romani S, Magee JC (2017) Inhibitory suppression of heterogeneously tuned excitation enhances spatial coding in CA1 place cells. Nat Neurosci 20:417-426.

Harvey CD, Collman F, Dombeck DA, Tank DW (2009) Intracellular dynamics of hippocampal place cells during virtual navigation. Nature 461:941-946.

Hill DN, Varga Z, Jia H, Sakmann B, Konnerth A (2013) Multibranch activity in basal and tuft dendrites during firing of layer 5 cortical neurons in vivo. Proc Natl Acad Sci U S A 110:13618-13623.

Hoffman DA, Magee JC, Colbert CM, Johnston D (1997) K+ channel regulation of signal propagation in dendrites of hippocampal pyramidal neurons. Nature 387:869-875.

Jahr CE, Stevens CF (1990) Voltage dependence of NMDA-activated macroscopic conductances predicted by single-channel kinetics. J Neurosci 10:3178-3182.

Jia H, Rochefort NL, Chen X, Konnerth A (2010) Dendritic organization of sensory input to cortical neurons in vivo. Nature 464:1307-1312.

Kleindienst T, Winnubst J, Roth-Alpermann C, Bonhoeffer T, Lohmann C (2011) Activity-dependent clustering of functional synaptic inputs on developing hippocampal dendrites. Neuron 72:1012-1024.

Lee D, Lin BJ, Lee AK (2012) Hippocampal place fields emerge upon single-cell manipulation of excitability during behavior. Science 337:849-853.

Losonczy A, Magee JC (2006) Integrative properties of radial oblique dendrites in hippocampal CA1 pyramidal neurons. Neuron 50:291-307.

Losonczy A, Makara JK, Magee JC (2008) Compartmentalized dendritic plasticity and input feature storage in neurons. Nature 452:436-441.

Magee JC (1998) Dendritic hyperpolarization-activated currents modify the integrative properties of hippocampal CA1 pyramidal neurons. J Neurosci 18:7613-7624.

Magee JC (2011) Observations on clustered synaptic plasticity and highly structured input patterns. Neuron 72:887-888.

Magee JC, Johnston D (1995) Characterization of single voltage-gated Na+ and Ca2+ channels in apical dendrites of rat CA1 pyramidal neurons. J Physiol 487 (Pt 1):67-90.

Magee JC, Johnston D (1997) A synaptically controlled, associative signal for Hebbian plasticity in hippocampal neurons. Science 275:209-213.

Makino H, Malinow R (2011) Compartmentalized versus global synaptic plasticity on dendrites controlled by experience. Neuron 72:1001-1011.

Marder E, Taylor AL (2011) Multiple models to capture the variability in biological neurons and networks. Nat Neurosci 14:133-138.

Migliore M, Hoffman DA, Magee JC, Johnston D (1999) Role of an A-type K+ conductance in the back-propagation of action potentials in the dendrites of hippocampal pyramidal neurons. J Comput Neurosci 7:5-15.

Milstein AD, Bloss EB, Apostolides PF, Vaidya SP, Dilly GA, Zemelman BV, Magee JC (2015) Inhibitory Gating of Input Comparison in the CA1 Microcircuit. Neuron 87:1274-1289.

Mukunda CL, Narayanan R (2017) Degeneracy in the regulation of short-term plasticity and synaptic filtering by presynaptic mechanisms. J Physiol 595:2611-2637.

Narayanan R, Johnston D (2007) Long-term potentiation in rat hippocampal neurons is accompanied by spatially widespread changes in intrinsic oscillatory dynamics and excitability. Neuron 56:1061-1075.

Narayanan R, Johnston D (2008) The h channel mediates location dependence and plasticity of intrinsic phase response in rat hippocampal neurons. J Neurosci 28:5846-5860.

Narayanan R, Johnston D (2010) The h current is a candidate mechanism for regulating the sliding modification threshold in a BCM-like synaptic learning rule. Journal of neurophysiology 104:1020-1033.

Narayanan R, Johnston D (2012) Functional maps within a single neuron. Journal of neurophysiology 108:2343-2351.

Prinz AA, Bucher D, Marder E (2004) Similar network activity from disparate circuit parameters. Nat Neurosci 7:1345-1352.

Pyapali GK, Sik A, Penttonen M, Buzsaki G, Turner DA (1998) Dendritic properties of hippocampal CA1 pyramidal neurons in the rat: intracellular staining in vivo and in vitro. J Comp Neurol 391:335-352.

Rall W (1977) Core conductor theory and cable properties of neurons. In: Handbook of physiology. The nervous system. Cellular biology of neurons (Kandel ER, ed), pp 39-97. Bethesda, MD: American physiological society.

Rathour RK, Narayanan R (2012a) Influence fields: a quantitative framework for representation and analysis of active dendrites. Journal of neurophysiology 107:2313-2334.

Rathour RK, Narayanan R (2012b) Inactivating ion channels augment robustness of subthreshold intrinsic response dynamics to parametric variability in hippocampal model neurons. J Physiol 590:5629-5652.

Rathour RK, Narayanan R (2014) Homeostasis of functional maps in active dendrites emerges in the absence of individual channelostasis. Proc Natl Acad Sci U S A 111:E1787-1796.

Regehr WG (2012) Short-term presynaptic plasticity. Cold Spring Harb Perspect Biol 4:a005702.

Regehr WG, Carey MR, Best AR (2009) Activity-dependent regulation of synapses by retrograde messengers. Neuron 63:154-170.

Schiller J, Schiller Y (2001) NMDA receptor-mediated dendritic spikes and coincident signal amplification. Current opinion in neurobiology 11:343-348.

Shah MM, Migliore M, Valencia I, Cooper EC, Brown DA (2008) Functional significance of axonal Kv7 channels in hippocampal pyramidal neurons. Proc Natl Acad Sci U S A 105:7869-7874.

Sheffield ME, Dombeck DA (2015) Calcium transient prevalence across the dendritic arbour predicts place field properties. Nature 517:200-204.

Sjostrom PJ, Rancz EA, Roth A, Hausser M (2008) Dendritic excitability and synaptic plasticity. Physiol Rev 88:769-840.

Spruston N, Schiller Y, Stuart G, Sakmann B (1995) Activity-dependent action potential invasion and calcium influx into hippocampal CA1 dendrites. Science 268:297-300.

Takahashi N, Kitamura K, Matsuo N, Mayford M, Kano M, Matsuki N, Ikegaya Y (2012) Locally synchronized synaptic inputs. Science 335:353-356.

Varga Z, Jia H, Sakmann B, Konnerth A (2011) Dendritic coding of multiple sensory inputs in single cortical neurons in vivo. Proc Natl Acad Sci U S A 108:15420-15425.

Watanabe S, Hoffman D, Migliore M, Johnston D (2002) Dendritic K+ channels contribute to spike-timing dependent long-term potentiation in hippocampal pyramidal neurons. Proc Natl Acad Sci USA 99:8366-8371.

Wilson DE, Whitney DE, Scholl B, Fitzpatrick D (2016) Orientation selectivity and the functional clustering of synaptic inputs in primary visual cortex. Nat Neurosci 19:1003-1009.

Winnubst J, Lohmann C (2012) Synaptic clustering during development and learning: the why, when, and how. Frontiers in molecular neuroscience 5:70.

FIGURE LEGENDS

Figure 1. Experimental constraints on the intrinsic and synaptic properties of a morphologically realistic CA1 pyramidal model neuron. (*A*) 2-dimensional projection of a 3-dimensional reconstructed hippocampal CA1 pyramidal neuron model used as the base model. (*B*) Experimentally constrained somatoapical distributions of active and passive parameters (Table 1) in the base model adopted from (Rathour and Narayanan, *PNAS*, 111, 2014) to match physiological measurements in *C–G*. (*C–G*) Backpropagating action potential (bAP) amplitude (*C*), input resistance (*D*, R_{in}), resonance frequency (*F*, f_R), total inductive phase (*G*, Φ_L) plotted as a function of radial distance from the soma. A chirp current stimulus, 100 pA in peak-to-peak amplitude and frequency linearly increasing from 0.1 Hz to 15 Hz in 15 s (*E*, top) was injected at the soma to record local voltage responses (*E*, bottom). The arrow marks the f_R. (*H–I*) *H* depicts the location-dependent permeability values of AMPA receptor that normalized somatic unitary postsynaptic potential (uEPSP) amplitudes to around 0.2 mV as depicted in *I*.

Figure 2. Place field synapses clustered on soma resulted in sharply-tuned place cells with disparate combinations of voltage-gated conductances. (*A*) Left to right sequence of plots: morphological reconstruction of the model with synaptic localization highlighted in green at soma; voltage traces obtained with 100 (red) and 500 (black) synapses; spike count plots (1 ms bin size) obtained from the voltage traces; firing rate profiles computed from the spike count plots. Note that the neuron enters a depolarization-induced block when N_{syn}=500. (*B*) Five example voltage traces (top) and corresponding firing rate profiles (bottom) of valid models showing similar tuning profiles. (*C*) Normalized

parameter values of model cells shown in *B* (same color code as *B*), showing disparate combinations of parameters yielding similar tuning in *B*. (*D*) FWHM and the corresponding F_{max} for all 5000 models generated through MPMOSS, plotted in ascending sequence of their FWHM values. Note that both the FWHMs and F_{max} span a small range for all models. (*E*) Scatter plot matrix and matrix representing corresponding Pearson's correlation coefficients (inset, left) for $N_{valid}=100$ models. The lowest row of boxes depicts the distribution of each parameter for all 5000 models. The correlation coefficient matrix plotted for $N_{valid}=5000$ models (inset, right) depicts a reduction in correlation coefficients with increase in N_{valid} (compared with inset, left). $N_{syn}=100$ for *B–E*.

Figure 3. Place field synapses clustered on one or two obliques yielded weak place cell tuning with low firing rates. (*A–B*) Left to right sequence of plots: morphological reconstruction of the model with synaptic localization highlighted in green; voltage traces obtained with the different number of synapses distributed with the same localization profile; spike count (1 ms bin size) plots; firing rate profiles. $N_{syn}=100$ (red), 500 (black). Plots correspond to synapses placed on a single apical oblique (*A*, *Ob1* branching from the trunk at ~160 μm from the soma) and synapses placed on two apical obliques (*B*, *Ob1* and *Ob2* branching from the trunk at ~160 μm and ~250 μm, respectively, from the soma).

Figure 4. Stochastic searches spanning densities of local subthreshold channels did not yield sharp place cell firing profiles when synapses were localized within a single oblique or two obliques. (*A*) Five example voltage traces (top) and corresponding firing

rate profiles (bottom) of cell models showing similar tuning profiles when synapses were clustered within a single oblique (*Ob1* in Fig. 3*A*). (*B*) Normalized parameter values of model cells shown in *A* (same color code as *A*), showing disparate combinations of parameters yielding similar tuning in *A*. (*C*) FWHM and corresponding F_{max} for all 5000 models generated through MPMOSS, plotted in ascending sequence of their FWHM values. (*D*) Scatter plot matrix and corresponding correlation coefficients (inset, left) for N_{valid}=74 similarly best-tuned models. The lowest row of boxes depicts the distribution of each parameter for all 5000 models. N_{syn}=100 for *A–D*. (*E–H*) Same as *A–D*, but with 50 synapses clustered on two different obliques (*Ob1* and *Ob2* in Fig. 3*B*) each. Scatter plots and correlation coefficients are for N_{valid}=46 similarly best-tuned models. In *D* and *H*, note that the correlation coefficient matrices plotted for N_{valid}=5000 models (inset, right) depicts a reduction in correlation coefficients with increase in N_{valid} (compared with inset, left).

Figure 5. Place field synapses randomly dispersed across the dendritic tree yielded sharply-tuned place cells with disparate combinations of active and passive parameters. (*A*) Left to right sequence of plots: morphological reconstruction of the model with synapses distributed throughout the proximal 300 μm of the apical dendritic arbor (green dots); voltage traces obtained with 100 (red) and 200 (blue) synapses; spike count plots (1 ms bin size); firing rate profiles. The two sets of red traces correspond to two different randomized distributions of 100 synapses. (*B*) Five example voltage traces (top) and corresponding firing rate profiles (bottom) of valid cell models, obtained from a stochastic search algorithm (N_{syn}=100) spanning passive and active properties (Table 2),

showing similar tuning profiles. (*C*) Normalized parameter values of model cells shown in *B* depicting disparate combinations of parameters yielding similar tuning in *B*.

Figure 6. Place field synapses randomly dispersed across the dendritic tree yielded sharply-tuned place cells with disparate combinations of active and passive parameters with weak pair-wise correlations. (*A*) Scatter plot matrix for N_{valid}=90 similarly best-tuned models, obtained with spatially dispersed place-field synapses (N_{syn}=100; Fig 5*A*), depicting pair-wise distributions between active and passive parameters (Table 2). The lowest row of boxes depicts the distribution of each parameter for these valid models. *Inset*, FWHM and corresponding F_{max} for the 90 valid models generated through MPMOSS, plotted in ascending sequence of their FWHM values. (*B*) Pearson correlation coefficient (*R*) matrix of the scatter plots in *A*. (*C*) Histogram of the correlation coefficients represented in *B*.

Figure 7. Models with place field synapses randomly dispersed across the dendritic tree exhibited characteristic excitatory voltage ramps, with the ramp amplitude and tuning sharpness dependent on the number of dispersed synapses. (*A*) Instantaneous firing rate profiles for four example valid cell models obtained with different numbers of randomly dispersed synapses. (*B–C*) Beeswarm plots of maximal firing frequency (F_{max}; *B*) and full-width at half maximum (FWHM; *C*) for all valid models (N_{valid} = 87), plotted as a function of number of dispersed synapses. The black rectangles depict the median for the corresponding data points. (*D*) *Left,* Median smoothed excitatory ramp (color-coded traces) overlaid on voltage traces (grey) of an example valid cell model activated with different number of synapses (represented on the left, with the color code). *Right,* For all

51

subpanels, the top traces depict magnified views of a shorter time window in the middle of the place field, depicting the theta modulation of the ramp (cyan traces). The bottom plots depict the frequency spectrum of the cyan trace (cyan traces for the entire 10 s time period on the left) also marking the frequency corresponding to the maximum power (black arrows). Although most models showed an excitatory ramp in the median filtered traces, in some models (100 synapses, right), the ramp-like depolarization was suppressed by the dominant afterhyperpolarization dynamics. (*E*) *Left,* Representative ramps for different numbers of synapses, same as ramp-like traces shown in *D*. *Right,* Beeswarm plots of maximum ramp voltages for all the valid models, plotted as a function of increasing number of synapses (N_{valid}=87). The black rectangles depict the medians for the corresponding cell population. The color codes for number of synapses are the same as *A–D*. (*F*) Histograms of maximum-power frequency in theta-smoothed ramps (cyan traces in *D*, and their power spectra there) for all the valid models as a function of number of synapses. For all plots in this figure, place field synapses were randomly dispersed.

Figure 8. Spatially dispersed synapses yielded sharply-tuned place cell models through dendritic spike initiation. (*A–D*) Color-coded schematic of the neuronal somato-apical arbor (left) showing various points where voltages (middle and right). N_{syn}=100 for all cases. *A–D* differ in terms of synaptic localization profiles: (*A*) All synapses clustered at soma. (*B*) All synapses clustered on one oblique. Shown is a representative non-propagating oblique dendritic spike (black arrow). (*C*) Synapses clustered at two obliques (50 each). (*D*) Synapses dispersed throughout the somatoapical arbor. For *C–D*, dendritic traces followed (top right) or preceded (bottom right) somatic

52

traces for different somatic action potentials. (*E*) Histograms of differences between the timing of somatic AP and dendritic bAP/dSpike along the somatoapical axis for the synaptic localization profiles analyzed in *A–D*. Note that negative values indicate the dendritic voltage peak preceding the somatic spike (dSpikes) whereas positive values indicate the somatic AP to precede all other dendritic locations (bAPs). (*F*) Plots, derived from the histograms in *E*, depicting the fraction of somatic APs where the dendritically recorded spike preceded the somatic AP. Note that the fraction of preceding dendritic spikes (dSpikes) was zero for all locations when synapses were localized to either the soma or a single oblique. (*G*) Amplitudes of the peak voltages along the somatoapical axis corresponding to the different synaptic localization profiles.

Figure 9. Place cell models with dispersed synaptic localization and disparate channel conductances lost sharpness of spatial tuning in the absence of dendritic sodium channels or NMDA receptors. (*A*) Schematic of the neuronal somato-apical arbor (left) showing various points where the voltages (middle) were recorded when sodium channels from apical dendrites were knocked out. Firing rate profiles for 4 different model cells (right lower panel) comparing neuronal responses in the presence (black dashed) and the absence (teal solid) of dendritic sodium channels. (*B*) Voltage traces recorded from various points along the somato-apical arbor (left; color code as in *A*) when NMDA receptors were knocked out across all synapses. Example dendritic voltage traces whose peaks followed (middle top) or preceded (right top) somatic peaks for two different somatic action potentials are depicted. In some cases dSpikes do not propagate to the soma to generate an action potential (middle bottom). Firing rate profiles for 4 different model cells (right lower panel) comparing neuronal responses in the

53

presence (black dashed) and the absence (maroon solid) of synaptic NMDARs. (*C–D*) Histograms of differences between the timing of somatic AP and dendritic bAP/dSpike along the somatoapical axis for the dendritic NaF⁻ and NMDAR⁻ cases. (*E*) Plots derived from the histograms in *C–D* depicting the fraction of somatic APs where the dendritically recorded spike preceded the somatic AP. (*F*) Amplitudes of the peak voltages along the somatoapical axis corresponding to control models and for the dendritic NaF⁻ and NMDAR⁻ cases. (*G–J*) Histograms (Left) and beeswarm plots (Right; adjacent rectangles indicate corresponding median values) of percentage changes in FWHM (*G*), F_{max} (*H*), area under the curve (AUC) (*I*), root mean square error (RMSE) of the firing rate profiles (*J*) obtained after virtual knockout of dendritic NaF and NMDARs from each of the 90 valid models in Fig. 6.

Figure 10. Virtual knockout of ion channels revealed the differential impact of different ion subthreshold channels on place cell tuning. (*A–D*) Histograms (Left) and beeswarm plots (Right; adjacent rectangles indicate corresponding median values) of percentage changes in FWHM (*A*), RMSE (*B*), F_{max} (*C*) and AUC (*D*) of the firing rate profiles, obtained after virtual knockout of different channels from each of the 87/90 valid models in Fig. 6. Black represents baseline measurements and channel knockouts are color-coded. Inset in *B* shows a representative firing rate profile of a valid model and the profile of the same model cell when different channels were knocked out.

Figure 11. Targeted synaptic plasticity in afferents from a specific place field was sufficient to elicit place-field selectivity in models that received randomly dispersed afferents from multiple place-field locations. (*A*) Five example voltage traces (top) and

corresponding firing rate profiles (bottom) of cell models that were valid. Note that the firing rate of these model cells within the second place field was at least 10 times larger than their firing rates within any of the other place fields. Provided are the peak in-field firing rate (F_{max}), FWHM and selectivity ratio (FR Ratio: ratio between the peak in-field and the peak out-of-field firing rates of the model) for all the five models. (*B*) Normalized parameter values of model cells shown in *A*, with identical color codes for individual models, showing disparate combinations of parameters yielding similar place-cell selectivity in *A*. (*C*) Histogram of the permeability folds (compared to base model permeability) for all the valid models (N_{valid}=60 models). (*D–F*) Scatter plot matrix (*D*) and matrix representing corresponding correlation coefficients (*E*) for the valid models, demonstrating weak pair-wise correlations across parameters. The lowest row of boxes in *D* depicts the distribution of each parameter for all the valid models. FWHM and corresponding F_{max} for the 60 valid models obtained through MPMOSS, plotted in ascending sequence of their FWHM values (inset in *D*). The histogram of correlation coefficients (*F*) in *E* confirmed the absence of any strong pairwise correlations between the parameters. The number of synapses was 50 for each of the five place fields, and were randomly dispersed across the dendritic arbor for all panels in the figure.

Table 1: Description of somatodendritic gradients in passive properties and channel gradients used in the model. x represents radial distance from the soma.

Parameter	Gradient of distribution
Specific membrane resistivity, R_m	$R_m(x) = R_m + \dfrac{(R_m\text{-min} - R_m\text{-max})}{1 + \exp((R_m\text{-hmp} - x)/R_m\text{-slope})} \, \text{k}\Omega/\text{cm}^2$
Axial resisitivity, R_a	$R_a(x) = R_a + \dfrac{(R_a\text{-min} - R_a\text{-max})}{1 + \exp((R_a\text{-hmp} - x)/R_a\text{-slope})} \, \Omega.\text{cm}$
Maximal conductance of NaF channels	$\overline{g}_{Na}$, uniform across the somatodendritic arbor, with the density at the axon initial segment set at $5\,\overline{g}_{Na}$
Maximal conductance of KDR channels	$\overline{g}_{KDR}$, uniform across the somatodendritic arbor
Maximal conductance of KA channels	$g_{KA}(x) = \overline{g}_{KA}\left(1 + \dfrac{\overline{g}_{KA}\text{-fold}}{100}\right) \, \text{mS/cm}^2$
Maximal conductance of h channels	$g_h(x) = \overline{g}_h\left(1 + \dfrac{\overline{g}_h\text{-fold}}{1 + \exp((\overline{g}_h\text{-hmp} - x)/\overline{g}_h\text{-slope})}\right) \, \mu\text{S/cm}^2$
Maximal conductance of CaT channels	$g_{CaT}(x) = \overline{g}_{CaT}\left(1 + \dfrac{\overline{g}_{CaT}\text{-fold}}{1 + \exp((\overline{g}_{CaT}\text{-hmp} - x)/\overline{g}_{CaT}\text{-slope})}\right) \, \mu\text{S/cm}^2$

56

Table 2: Model parameters and their base values for the model. Refer to Table 1 for the specific formulations of each passive/active gradient mentioned below.

| No.	Parameter (unit)	Symbol	Base value
R_a distribution			
1	Minimum value (Ω.cm)	R_a-soma	120
2	Maximum value (Ω.cm)	R_a-end	70
3	Half-maximal point of sigmoid (μm)	R_a-hmp	300
4	Slope of sigmoid (μm)	R_a-slope	50
R_m distribution			
5	Minimum value (kΩ/cm^2)	R_m-soma	125
6	Maximum value (kΩ/cm^2)	R_m-end	850
7	Half-maximal point of sigmoid (μm)	R_m-hmp	300
8	Slope of sigmoid (μm)	R_m-slope	50
Properties of spiking conductances			
9	Maximal conductance of fast sodium channel (mS/cm^2)	$\overline{g}_{Na}$	16
10	Maximal conductance of delayed rectifier potassium channel (mS/cm^2)	$\overline{g}_{KDR}$	10
h channel properties			
11	Maximal somatic conductance (μS/cm^2)	$\overline{g}_h$	25
12	Fold increase	$\overline{g}_h$-fold	12
13	Half-maximal point of sigmoid (μm)	$\overline{g}_h$-hmp	320
14	Slope of sigmoid (μm)	$\overline{g}_h$-slope	50
T-type Ca^{2+} channel properties			
15	Maximal somatic conductance (μS/cm^2)	$\overline{g}_{CaT}$	80
16	Fold increase	$\overline{g}_{CaT}$-fold	30
17	Half-maximal point of sigmoid (μS/cm^2)	$\overline{g}_{CaT}$-hmp	350
18	Slope of sigmoid (μm)	$\overline{g}_{CaT}$-slope	50
A-type K$^+$ channel properties			
19	Maximal somatic conductance (mS/cm^2)	$\overline{g}_{KA}$	3.1
20	Fold increase per 100 μm	$\overline{g}_{KA}$-fold	8

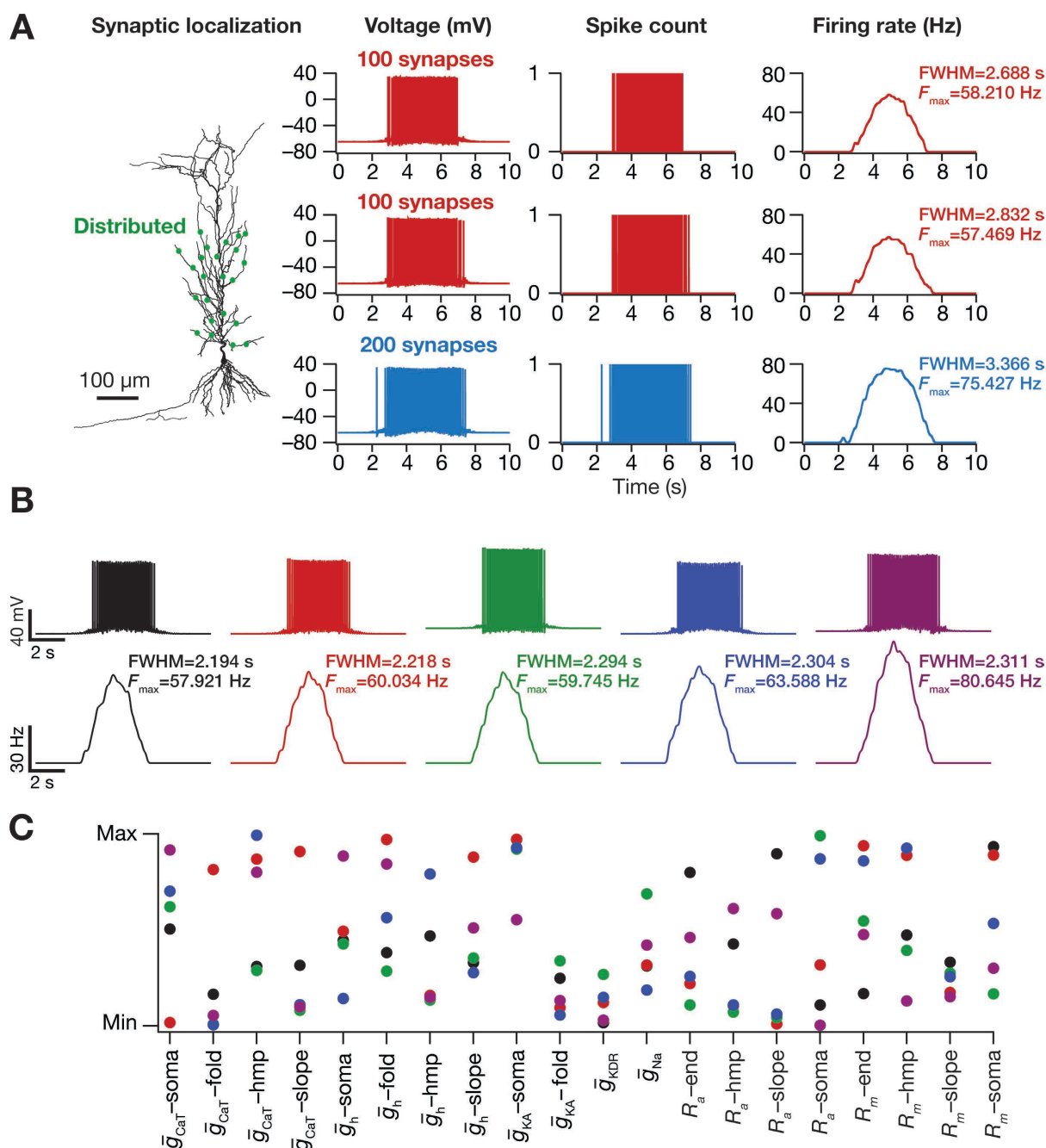57
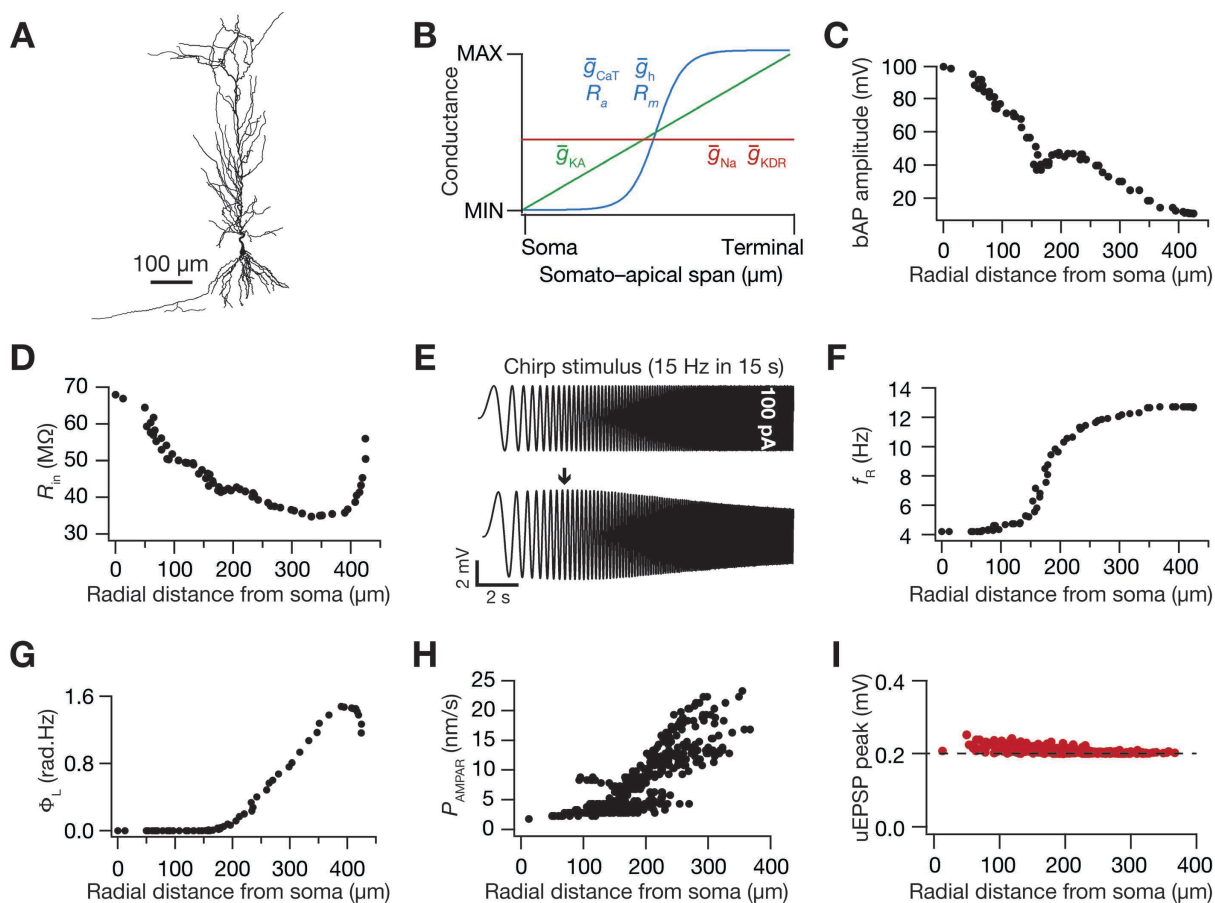
Basak and Narayanan: Figure 1
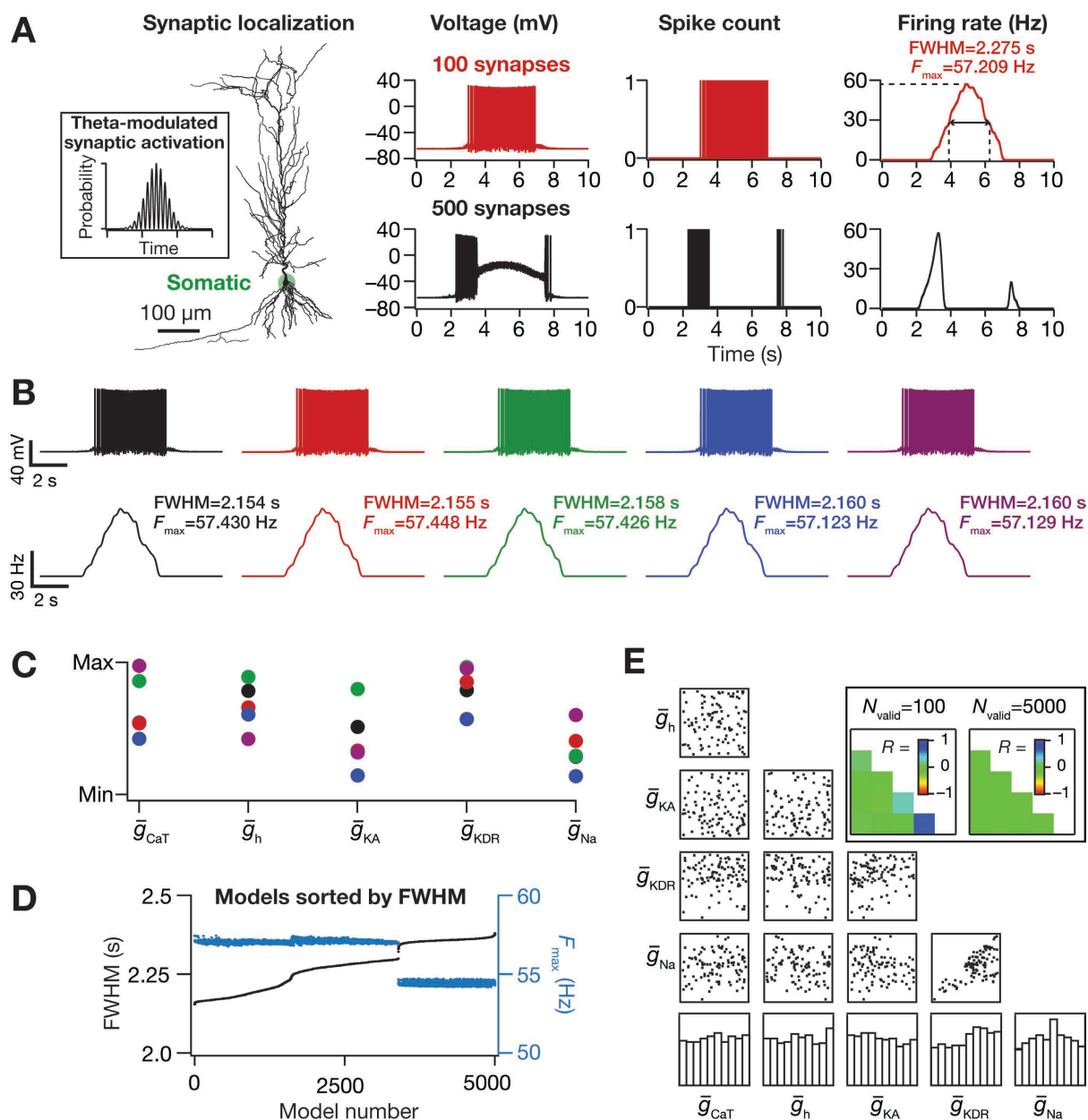
Basak and Narayanan: Figure 2
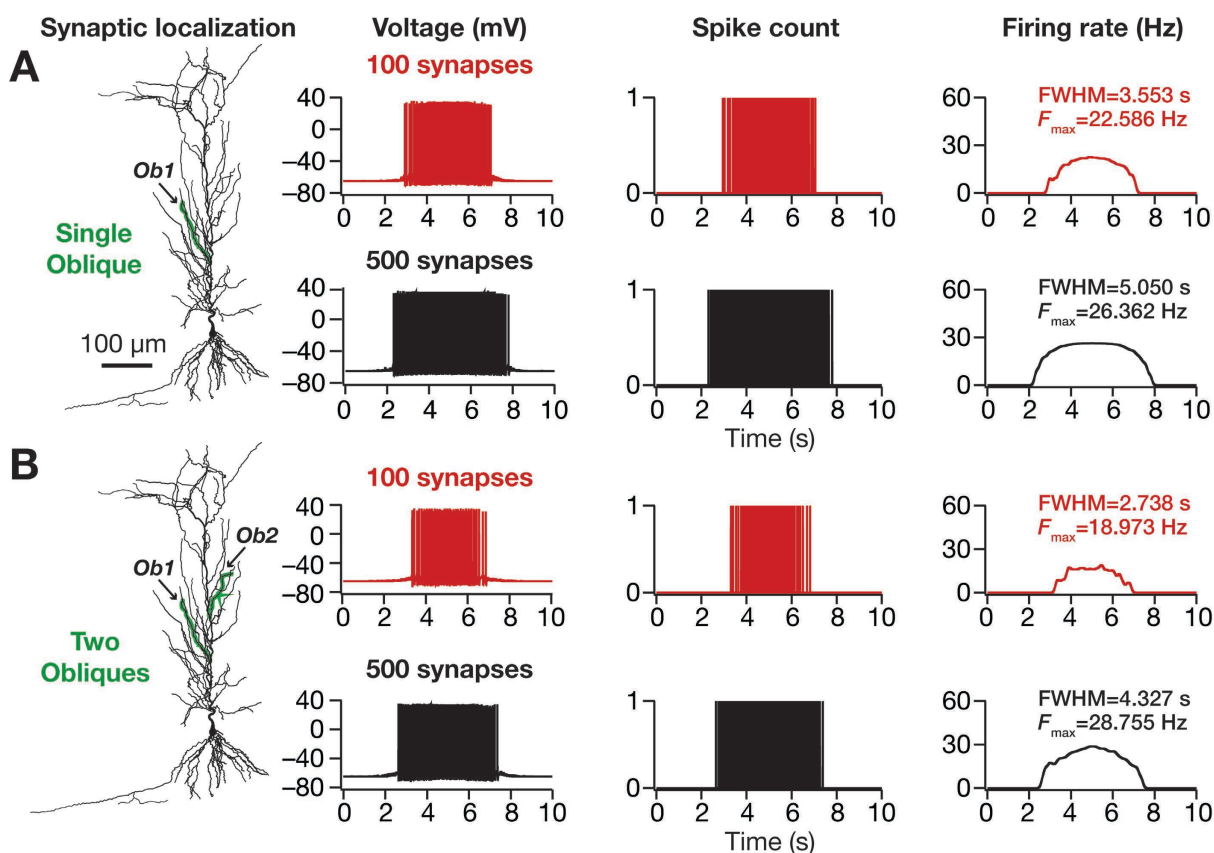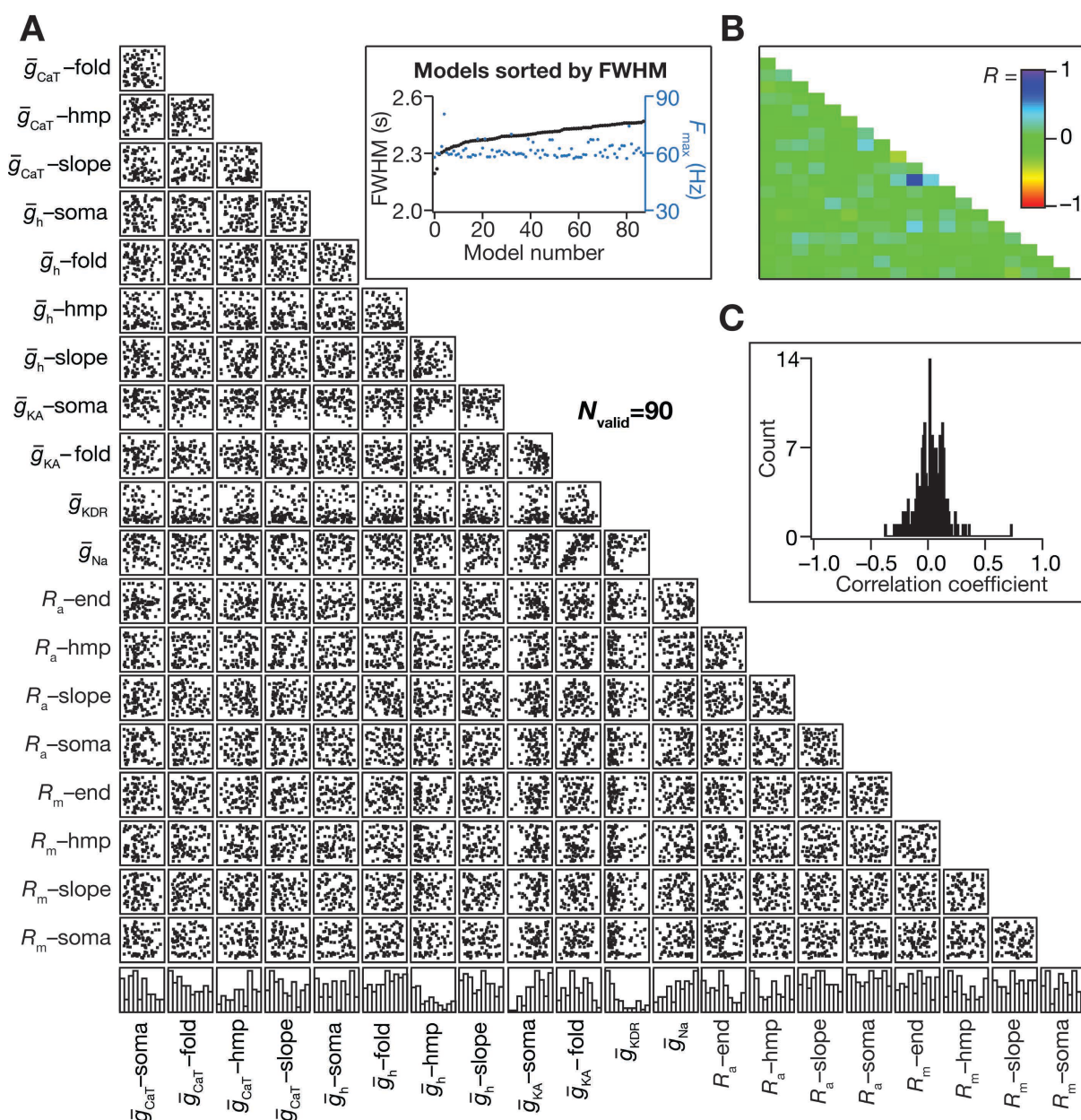
Basak and Narayanan: Figure 3
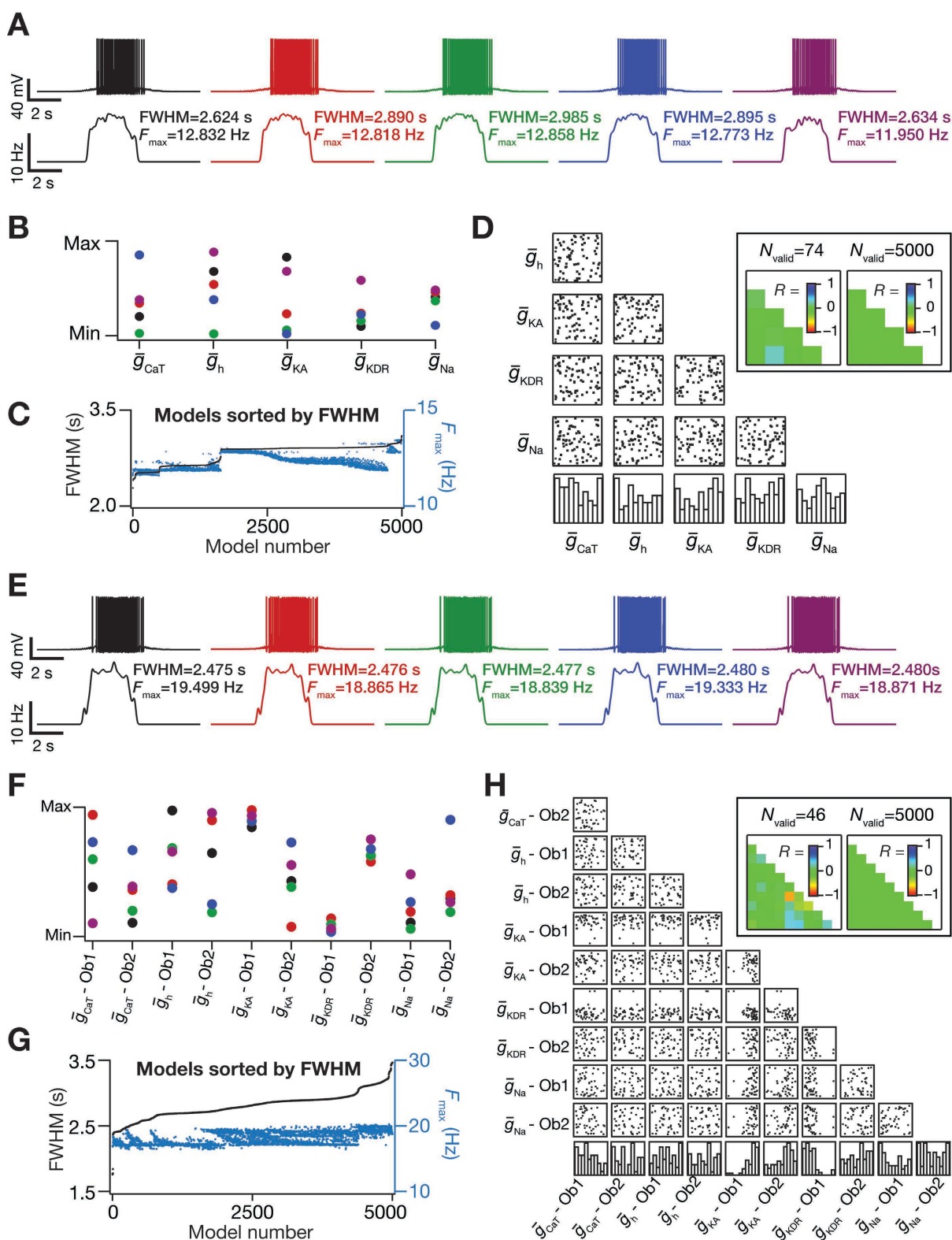
Basak and Narayanan: Figure 4

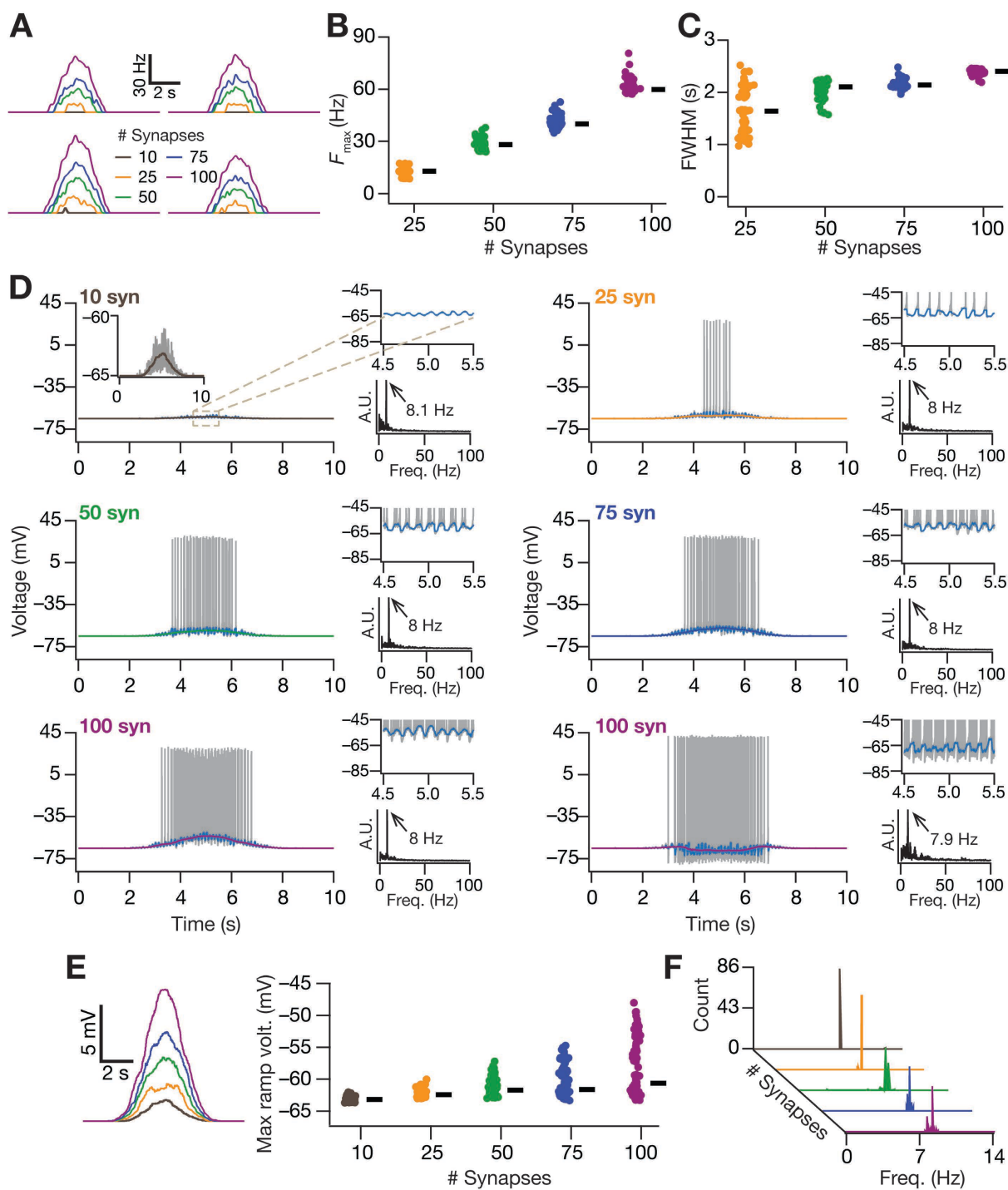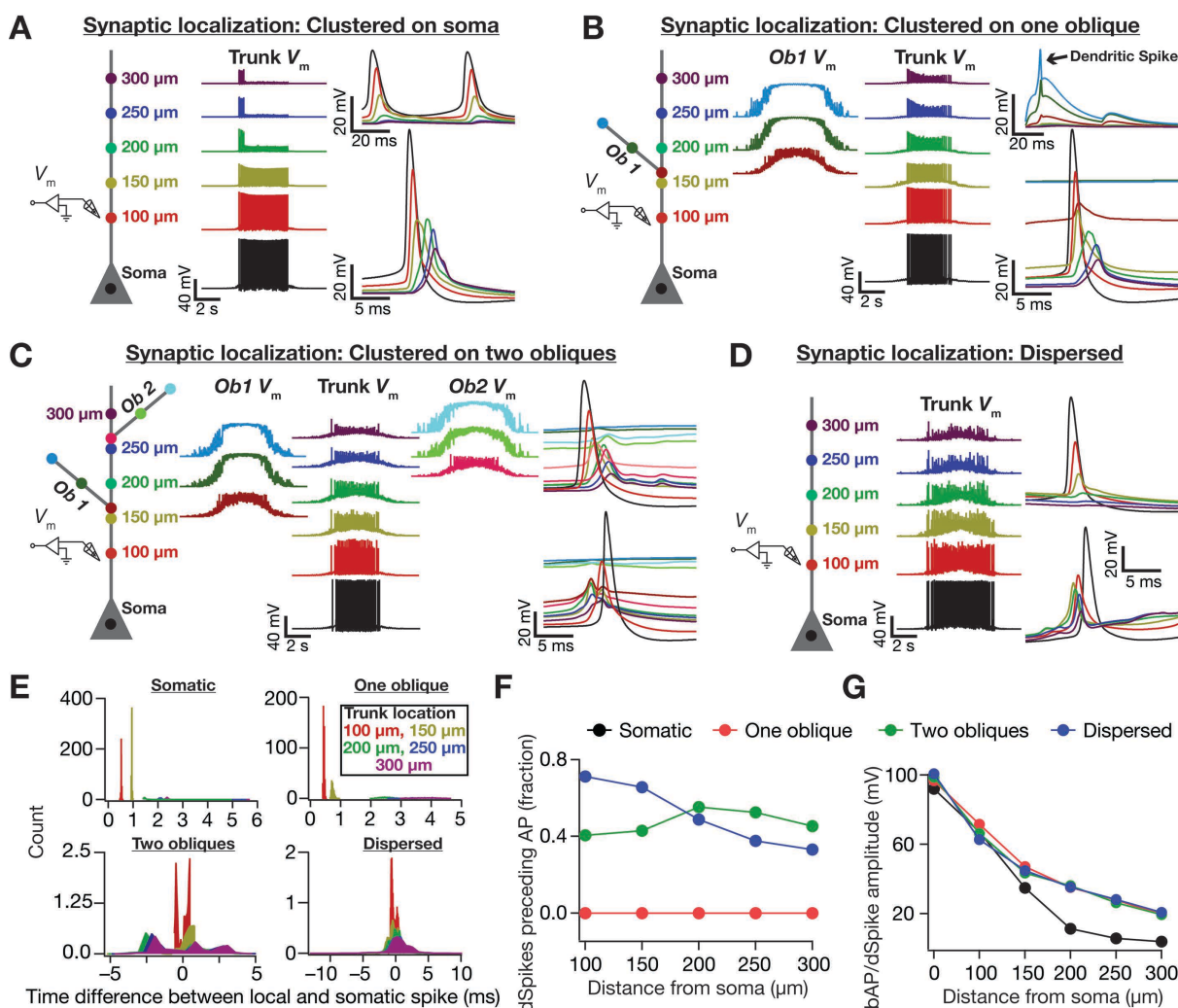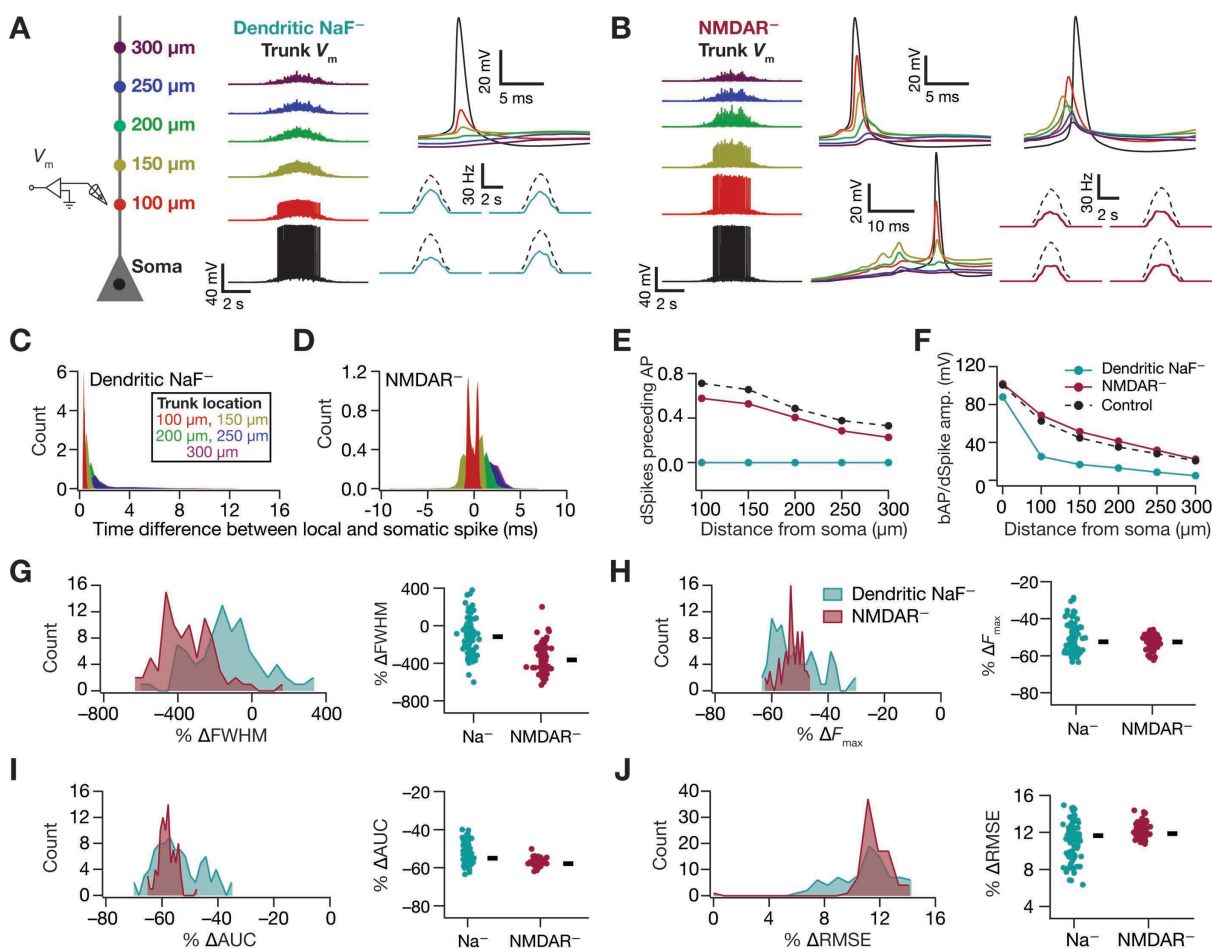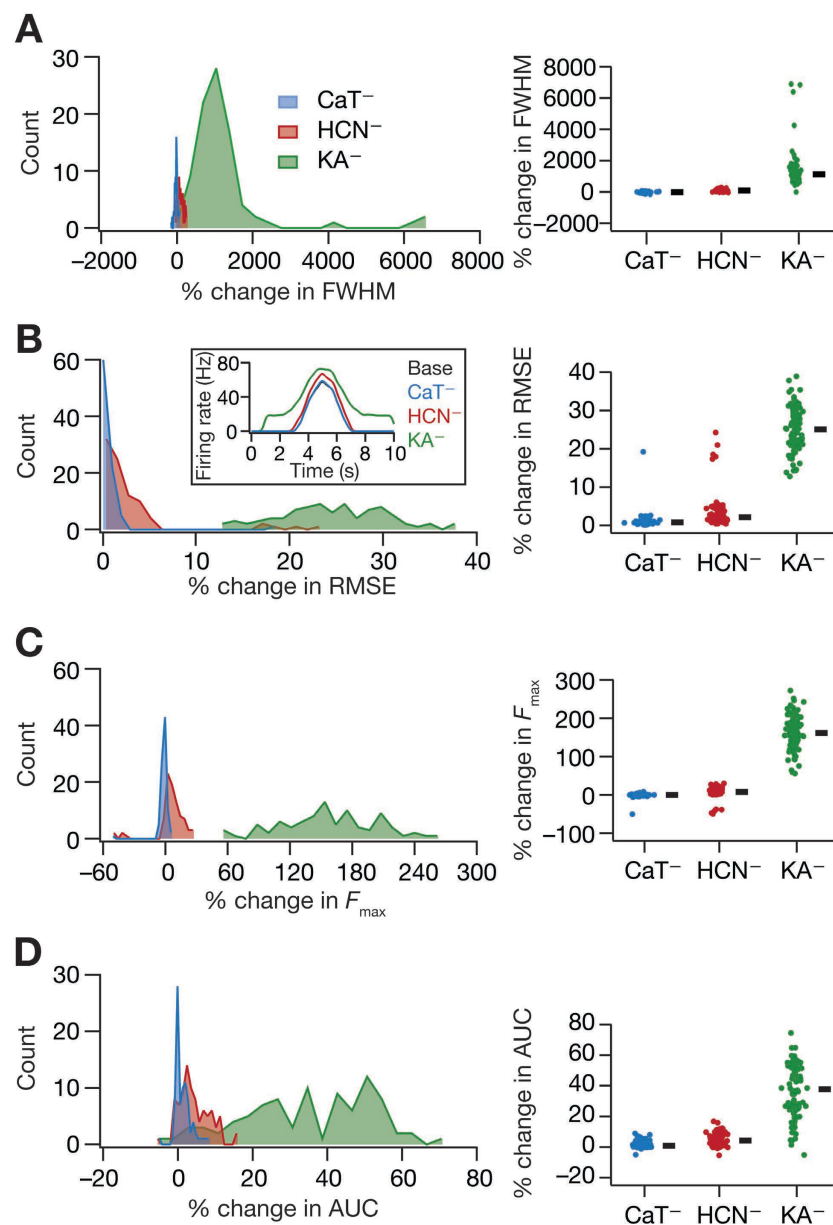**Basak and Narayanan: Figure 5**

Basak and Narayanan: Figure 6

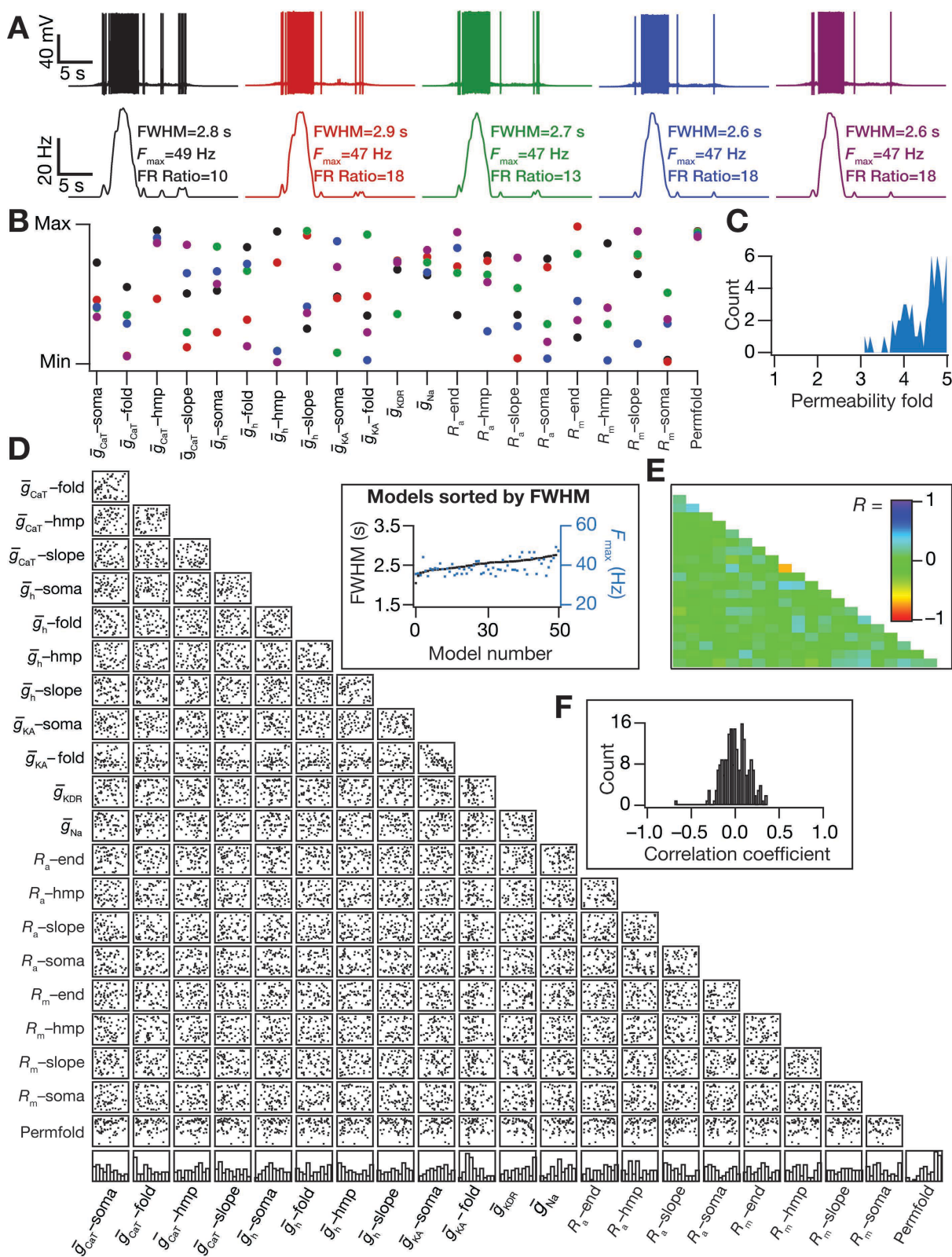**Basak and Narayanan: Figure 7**

Basak and Narayanan: Figure 8

Basak and Narayanan: Figure 9

Basak and Narayanan: Figure 10

Basak and Narayanan: Figure 11